

# Super-Resolution 3-D Microwave Imaging of Objects With High Contrasts by a Semijoin Extreme Learning Machine

Li-Ye Xiao<sup>ID</sup>, Member, IEEE, Jiawen Li, Feng Han<sup>ID</sup>, Senior Member, IEEE, Hao-Jie Hu, Mingwei Zhuang<sup>ID</sup>, and Qing Huo Liu<sup>ID</sup>, Fellow, IEEE

**Abstract**—This article proposes a semijoin extreme learning machine (SJ-ELM) for super-resolution 3-D microwave imaging of objects with high contrasts. The proposed scheme develops a shallow neural network structure with the semijoin strategy to convert the scattered field data into two output channels, namely, the permittivity and the conductivity of objects, respectively. The semijoin strategy can decrease the inner matrix dimensions to reduce the computational burden for 3-D super-resolution imaging, so it is employed to connect between the nodes of the hidden layer and the output layer. The imaging performance of the proposed SJ-ELM and the conventional variational Born iterative method (VBIM) is first compared for imaging objects with different electrical sizes and contrasts, and then, different targets of imaging resolution are designed to evaluate both solvers. The proposed SJ-ELM is also assessed for imaging objects with high contrasts and experimental data and is demonstrated to have superior super-resolution imaging capabilities for high-contrast 3-D objects.

**Index Terms**—Extreme learning machine (ELM), high contrast, microwave imaging (MWI), super-resolution.

## I. INTRODUCTION

AS AN electromagnetic inverse scattering problem, microwave imaging (MWI), which is a noninvasive and nondestructive technique to inspect materials by using incident electromagnetic waves generated in the microwave range, has gained a lot of interest recently. The capabilities of microwaves in penetrating dielectric materials have led this diagnostic technique to be proposed in several application scenarios, such as biomedical imaging [1]–[8], through-wall imaging [9], airport security [10]–[12], and geophysical inspection [13]–[17].

Manuscript received February 25, 2021; revised May 10, 2021, June 8, 2021, and June 19, 2021; accepted June 26, 2021. Date of publication August 9, 2021; date of current version November 4, 2021. This work was supported in part by the National Postdoctoral Program for Innovative Talents under Grant BX2019018, in part by the National Key Research and Development Program of China under Grant 2018YFC0603503, and in part by the National Natural Science Foundation of China under Grant 62001406 and Grant 61871462. (*Corresponding authors:* Qing Huo Liu; Mingwei Zhuang.)

Li-Ye Xiao, Jiawen Li, Feng Han, Hao-Jie Hu, and Mingwei Zhuang are with the Institute of Electromagnetics and Acoustics, School of Electronic Science and Engineering, Xiamen University, Xiamen 361005, China (e-mail: liyexiao16@gmail.com; mw.zhuang@xmu.edu.cn).

Qing Huo Liu is with the Department of Electrical and Computer Engineering, Duke University, Durham, NC 27708 USA (e-mail: qhliu@duke.edu).

Color versions of one or more figures in this article are available at <https://doi.org/10.1109/TMTT.2021.3100421>.

Digital Object Identifier 10.1109/TMTT.2021.3100421

Due to the intrinsic nonlinearity of the inverse scattering problem and the ill-posedness of the discretized matrix equations, it is a challenging task to find a reliable, accurate, and numerically efficient inversion method [9]. Usually, MWI could be classified as quantitative and qualitative [6].

Qualitative MWI, which sacrifices the accuracy in favor of computational speed, could give the approximate shapes and locations of the unknown targets with low computational costs. Therefore, in many scenarios where the real-time results are necessary, qualitative MWI is always adopted. Afsari *et al.* [18] proposed a fast medical microwave tomography algorithm that could be potentially used in emergency medical scenarios, such as professional sports or road accidents. The back-projection (BP) tomography [19] and diffraction tomography [20] were adopted in real-time through-wall imaging. Another important application is synthetic aperture radar (SAR). It has been used to image the earth's surface [21], [22] or detect moving targets [23]. However, qualitative MWI only gives the images of the targets and cannot be used to retrieve their dielectric properties.

For the quantitative MWI, more model parameters of the unknown targets, including shapes, positions, and dielectric parameters, could be obtained. Usually, according to the minimization procedure of the cost function, quantitative methods could be classified into the deterministic inversion method and the stochastic inversion method [13]. Nonlinear methods, such as the subspace optimization method (SOM) [25], [26], the contrast source-type inversion (CSI) method [27]–[30], and the Born iterative method (BIM) [24] and its variants, are the commonly used deterministic methods that could reconstruct the model parameters of the unknown objects through minimizing the misfit between the calculated and measured scattered field data iteratively.

The stochastic methods, such as the genetic algorithm (GA) [31]–[33], the particle swarm optimization (PSO) [34]–[36], and the memetic algorithm (MA) [37], have also been applied to MWI [38]. Compared with the deterministic method, the stochastic method can avoid being trapped into the local minima of the cost function. However, for the stochastic method, the dimension of unknown model parameters is severely restricted and, thus, is especially problematic for the 3-D voxel-based inversion in which the dielectric parameters in all discretized cells need to be retrieved.

In recent years, combined with machine learning techniques, some new methodologies have been proposed to reconstruct the shapes, positions, and dielectric parameters of the unknown targets [39], [40]. The pixel/voxel-based method, where the value of the dielectric parameter of each pixel/voxel is an independent parameter, could conveniently present any number of spatially inhomogeneous objects for the 2-D and 3-D problems, respectively; thus, this kind of method has attracted more and more attention and studies. A novel deep learning neural network architecture, termed DeepNIS, is proposed for 2-D objects inversion in [41]. In DeepNIS, the back-propagation method algorithm is first employed to generate complex-valued images as the inputs of a cascade of three convolutional neural network modules; then, CNN modules are used to improve the image quality one by one and output the dielectric parameter distribution of the imaging domain. With the verification of several representative tests, the DeepNIS has a better performance in terms of both the reconstruction accuracy and computational time, compared with conventional nonlinear inverse scattering methods. Based on U-Net, three schemes, the direct inversion scheme (DIS), the BP scheme (BPS), and the dominant current scheme (DCS), are proposed and compared for 2-D objects inversion in [42]. In terms of the results of simulated and experimental data, the proposed DCS outperforms the other two schemes. In [43], an inversion method based on the Born approximation (BA) and a 3-D U-Net is proposed for 3-D object inversion, where BA is employed to produce the preliminary 3-D images as the input of 3-D U-Net.

Usually, solving a 3-D super-resolution imaging problem with high-contrast objects requires either large memory storage and/or expensive computation. The deterministic methods are quite sensitive to initial guesses obtained from linearized approximation. When the objects have high contrasts, the deterministic methods will fail. Meanwhile, in such 3-D problems, the stochastic optimization methods require quite a huge computational cost, including CPU time and memory. Furthermore, as the input of the traditional machine learning methods (such as DeepNIS, BPS, and DCS) is also obtained from a linearized approximation, when the contrasts of objects are high, it is hard to obtain desired input from the linearized approximation. In addition, the DIS in [42] can directly map scattered field data to the object parameter distribution; however, as explained in [42], due to the unmatched model structure, the accuracy is not ideal. Meanwhile, the methods proposed in these studies are devoted to solve 2-D inverse scattering problems. Although the BA-3-D U-Net model [43] could reconstruct 3-D objects, the input of 3-D U-Net is still based on the linearized approximation, BA, which is incapable of imaging high-contrast objects. Thus, how to solve 3-D super-resolution imaging problems with high-contrast objects is still a challenging task.

In this article, a semijoin extreme learning machine (SJ-ELM) solver is proposed for quantitative super-resolution imaging of 3-D objects with high contrasts. The extreme learning machine (ELM), as a single-hidden layer feed-forward neural network (SLFNN), is suitable for nondifferential activation functions; to a large extent, it prevents some troubling

issues, such as stopping criteria, learning rate, training epochs, and local minima [44]. Different from most neural networks, ELM only needs to solve the matrix between the hidden layer and the output layer. This is the merit of the ELM. Compared with the traditional ELM, there are two hidden layers in SJ-ELM. Meanwhile, based on the semijoin strategy, the nodes in the hidden layer of SJ-ELM are not totally connected to the nodes in the output layer, so both the inner matrix dimensions and required memory storage of SJ-ELM are less, and the convergence of the model is faster. In the proposed scheme, two channels are employed for mapping permittivity and conductivity of objects, respectively, through converting the scattered field data by using the semijoin strategy. The proposed scheme is different from DeepNIS in [41], BPS and DCS in [42], and BA-3-D U-Net in [43] since the preliminary image of model parameter distribution in these three schemes is first obtained by linear approximations, e.g., BP or BA, and then, deep learning neural networks, such as CNN or U-Net, are employed to map the preliminary image to the final reconstructed results. For the proposed model, the scattered field data can be directly mapped to the distribution of object parameters even though the final reconstructed objects have high contrasts.

Meanwhile, the proposed SJ-ELM also differs from our previous work in 2-D [45] in which this work can reconstruct the permittivity and the conductivity of 3-D objects in two channels. Furthermore, in [45], the nonlinear mapping module (NMM) part is based on the full-join ELM architecture. Unfortunately, this kind of architecture is not suitable for 3-D problems because of its unacceptably high computational cost. The main contributions of the proposed SJ-ELM can be summarized as follows. First, to reduce the computational burden for super-resolution imaging, a novel semijoin strategy is proposed to set the connection between the nodes of the hidden layer and the output layer of SJ-ELM. Meanwhile, the semijoin strategy can improve the convergence performance of the solver. On the other hand, this strategy decreases the inner matrix dimensions, thus requiring less memory storage compared with the traditional full-join strategy. The detailed description is shown in Section III. Second, the proposed SJ-ELM can conduct 3-D super-resolution imaging of high-contrast objects due to the convergence guarantee from the semijoin strategy. So far, this kind of imaging problem is always been a challenging task in electromagnetic inversion. It is worth mentioning that SJ-ELM is only constructed with shallow neural networks based on the ELM, which has low training costs compared with the deep learning model for a 3-D imaging problem.

This article is organized as follows. In Section II, the formulation of MWI based on integral equations is briefly reviewed. In Section III, the proposed SJ-ELM is discussed in detail. In Sections IV and V, tests with numerical and experimental data are, respectively, conducted. Finally, we summarize this article in Section VI.

## II. CONVENTIONAL SOLUTIONS OF MWI

Through-wall imaging is an important application of MWI. Thus, this article mainly considers this layered medium case.

The forward model for EM scattering in a layered medium is formulated by the state equation, which can be expressed as a volume integral

$$\mathbf{E}_{\text{inc}}^n = \mathbf{E}_{\text{tot}}^n - j\omega\epsilon_b \int_D \overline{\mathbf{G}}_{\text{EJ}}^{nm}(\mathbf{r}, \mathbf{r}') \cdot \chi(\mathbf{r}') \mathbf{E}_{\text{tot}}^m(\mathbf{r}') d\mathbf{r}' \quad (1)$$

where  $\chi = (\epsilon - \epsilon_b)/\epsilon_b$  is the contrast function of the objects,  $\epsilon_b$  is the permittivity of the background medium in the  $m$ th layer,  $\omega$  is the angular frequency,  $\mathbf{E}_{\text{inc}}^n$  is the incident electric field in the  $n$ th layer, and  $\mathbf{E}_{\text{tot}}^n$  and  $\mathbf{E}_{\text{tot}}^m$  are the total electric field in the  $n$ th and  $m$ th layers, respectively. The inversion model is formulated by the data equation [46], [47], which can be expressed as

$$\mathbf{E}_{\text{sct}}^n(\mathbf{r}) = j\omega\epsilon_b \int_D \overline{\mathbf{G}}_{\text{EJ}}^{nm}(\mathbf{r}, \mathbf{r}') \cdot \chi(\mathbf{r}') \mathbf{E}_{\text{tot}}^m(\mathbf{r}') d\mathbf{r}' \quad (2)$$

where  $\overline{\mathbf{G}}_{\text{EJ}}^{nm}$  is the layered medium dyadic Green's function (DGF) [48] connecting the equivalent electric current sources in the  $m$ th layer and the receivers in the  $n$ th layer, and  $D$  is the computation domain enclosing the scatterers and located in the  $m$ th layer. In the forward scattering computation, (1) is discretized, and  $\mathbf{E}_{\text{tot}}^m$  in the  $m$ th layer is solved by the stabilized biconjugate gradient fast Fourier transform (BCGS-FFT) method [49].

In the inverse scattering computation, (2) is discretized, and the model parameter  $\chi$  is usually solved by the variational Born iterative method (VBIM) [45], [47] or other traditional nonlinear inverse scattering methods. This iteration continues until the misfit between the measured scattered field and the model calculated field reaches a stop criterion. In this work, we will propose the SJ-ELM solver to solve this inverse problem and compare it with VBIM.

One should note that the discretization in the forward solver is different from the discretization in the inversion scheme. For the forward solver, the discretization should satisfy the requirement of forward calculation in terms of the sampling density. In the inversion, the discretization of the imaging domain mainly depends on the requirement of imaging resolution and computational cost.

### III. PROPOSED SJ-ELM MODEL

#### A. Semijoin Extreme Learning Machine

Compared with the full-joint strategy in the traditional ELM [44], for the semijoin strategy, the nodes in the hidden layer are not totally connected to the nodes in the output layer, so both the inner matrix dimensions and required memory storage of SJ-ELM are less, and the convergence of the model is faster. To relieve the convergence stress of the machine learning method during the inversion process, as shown in Fig. 1, the permittivity and the conductivity are conducted to inverse with two separate channels, respectively. The scattered fields obtained from the forward solver are complex value data, while the relative permittivity and conductivity of each channel are real values. Thus, each channel is employed to convert the complex scattered field data to the real permittivity and conductivity values with a simple structure and low training cost, respectively. However, the outputs of two channels will

be composed of the complex permittivity as the final inversion result of the proposed SJ-ELM.

Both channels have the same structure, and each channel consists of four layers, i.e., an input layer, two hidden layers, and an output layer. In each channel, each hidden layer receives the output of the previous layer in input and transmits it to the next layer. The input of the  $j$ th training sample is a column vector  $x_j = [x_{1j}, x_{2j}, \dots, x_{mj}]^T \in \mathbf{C}^m$  which contains the complex values  $E_x^{\text{sct}}$ ,  $E_y^{\text{sct}}$ , and  $E_z^{\text{sct}}$  for all the transmitter and receiver combinations to the permittivity or conductivity distribution in 3-D space, where  $m$  is the input dimension of the  $j$ th training sample,  $j = 1, 2, \dots, P$ , and  $P$  presents the total set number of training data. The whole imaging space is discretized into  $N_1$ ,  $N_2$ , and  $N_3$  voxels in the  $x$ -,  $y$ -, and  $z$ -directions. Correspondingly, for the target of the  $j$ th training set, the corresponding  $j$ th output of the  $j$ th training sample could be expressed as a column matrix  $\mathbf{o}_j = [o_{1j}, o_{2j}, \dots, o_{N_1 \times N_2 \times N_3, j}]^T \in \mathbf{R}^{(N_1 \times N_2 \times N_3) \times 1}$ , where  $N_1 \times N_2 \times N_3$  is the total number of voxels in the imaging domain. Usually, in the 3-D super-resolution imaging,  $N_1 \times N_2 \times N_3$  is a huge number, which will bring an unacceptable burden for computer memory. Thus, in the proposed semijoin strategy, the output matrix is uniformly divided into  $N$  subsets, which could be described as  $\mathbf{o}_j = \mathbf{o}_j^1 \cup \dots \cup \mathbf{o}_j^N \dots \cup \mathbf{o}_j^N$ , where  $\mathbf{o}_j^n \in \mathbf{R}^{((N_1 \times N_2 \times N_3)/N) \times 1}$ . For the convenient description, here, we set  $(N_1 \times N_2 \times N_3)/N = F$ . After many numerical experiments and analyses,  $N$  is recommended to set as the maximum value of  $N_1$ ,  $N_2$ , and  $N_3$ .

An input layer with  $m$  nodes, a complex-valued hidden layer with  $L$  nodes, a real-value hidden layer with  $S$  nodes, and an output layer with  $F$  nodes are contained in SJ-ELM. The calculation of the  $n$ th subset could be expressed as

$$\mathbf{o}_j^n = \overline{\boldsymbol{\alpha}}^n g_r \left( \overline{\mathbf{w}}_r^n \cdot \left| \overline{\boldsymbol{\beta}}^n g_c \left( \overline{\mathbf{w}}_c^n \cdot \mathbf{x}_j + \mathbf{b}^n \right) \right| + \mathbf{p}^n \right). \quad (3)$$

From the input layer to the first hidden layer,  $\overline{\mathbf{w}}_c^n$ ,  $\mathbf{b}^n$ ,  $\overline{\boldsymbol{\beta}}^n$ , and  $g_c$  are involved.  $\overline{\mathbf{w}}_c^n$ , which is an  $L \times m$  complex-valued random weight matrix, connects the input layer and the first hidden layer.  $\mathbf{b}^n$ , which is  $L$  complex-valued random column vector, presents the threshold of the first hidden layer.  $\overline{\boldsymbol{\beta}}^n$  is an  $F \times L$  complex-valued matrix that connects the complex-valued hidden layer to the real-value hidden layer. Its elements will be determined in the training.  $g_c$  is the nonlinear activation function of the first hidden layer, and its output is the  $L$  complex value numbers in the nodes of the first hidden layer.

From the first hidden layer to the second hidden layer,  $\overline{\mathbf{w}}_r^n$ ,  $\mathbf{p}^n$ ,  $\overline{\boldsymbol{\alpha}}^n$ , and  $g_r$  are involved.  $\overline{\mathbf{w}}_r^n$  is  $S \times F$  real-value random matrix as the weight matrix between the first hidden layer and the second hidden layer.  $\mathbf{p}^n$  is a vector with  $S$  real-value random numbers.  $\overline{\boldsymbol{\alpha}}^n$  is an  $F \times S$  real-value random matrix, which is the weights connecting the nodes in the second hidden layer and the output layer.  $g_r$  is the real-value activation function of the second hidden layer.

Based on our previous study [45], the inverse hyperbolic function and the sigmoid function expressed in the following:

$$g_c(x) = \arcsin h(x) = \int_0^x \frac{dt}{\left[ (1+t^2)^{1/2} \right]} \quad (4)$$

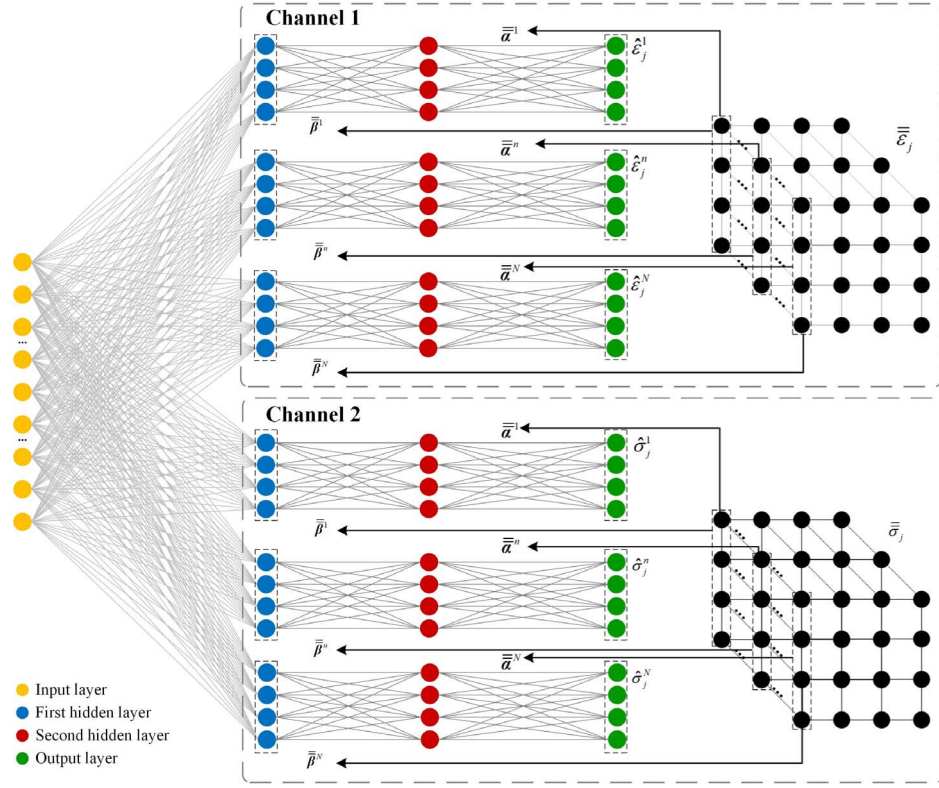


Fig. 1. Structure of the proposed SJ-ELM scheme, which consists of two channels for mapping the relative permittivity and conductivity distributions of objects, respectively. Both channels have the same structure, and each channel consists of four layers, i.e., an input layer, two hidden layers, and an output layer.  $\bar{\alpha}^n$  and  $\bar{\beta}^n$  are the weight matrix of both hidden layers for the  $n$ th subset, and they could be obtained from the target as shown by arrows, respectively.

$$g_r(x) = \text{sigmoid}(x) = \frac{1}{1 + e^{-x}} \quad (5)$$

are the complex activation function  $g_c$  for the first hidden layer and the real activation function  $g_r$  for the second hidden layer, respectively.

According to the ELM theory [44], [50]–[52], the initial values of  $\bar{\mathbf{w}}_c^n$ ,  $\mathbf{b}^n$ ,  $\bar{\mathbf{w}}_r^n$ , and  $\mathbf{p}^n$  are set randomly. Here, “random” means that the elements in the weight matrices are randomly generated instead of being obtained in the training. The training cost is low since we only need to solve the matrices  $\bar{\beta}^n$  and  $\bar{\alpha}^n$ .

Assume that the corresponding true permittivity or conductivity values of the  $n$ th subset of the  $j$ th training sample are denoted as  $t_j^n$ . Let  $\sum_{j=1}^P \|\mathbf{o}_j^n - t_j^n\| = 0$ , and employ layer-by-layer solving strategy to obtain the weight matrices  $\bar{\alpha}^n$  and  $\bar{\beta}^n$  of both hidden layers for the  $n$ th subset, respectively, where the second hidden layer is employed to make the model further converge to the target based on the results from the first hidden layer. The relationship between the weight matrix  $\bar{\beta}^n$  of the first hidden layer and  $t^n$  can be compactly expressed as

$$\bar{\beta}^n g_c^n = t^n, \quad n = 1, \dots, N \quad (6)$$

where the complex-valued matrix  $g_c^n = (\bar{\mathbf{w}}_c^n \cdot \mathbf{x}_j + \mathbf{b}^n)_{L \times P}$  is the first hidden layer output matrix. Thus, the desired complex weight matrix of  $\bar{\beta}^n$  can be obtained by the following equation:

$$\hat{\beta}^n = t^n g_c^{n\dagger}, \quad n = 1, \dots, N \quad (7)$$

where the complex matrix  $g_c^{n\dagger}$  presents the Moore–Penrose generalized inverse of the complex matrix  $g_c^n$ . The relationship between the weight matrix  $\bar{\alpha}^n$  of the second hidden layer and  $t^n$  can be compactly expressed as

$$\bar{\alpha}^n g_r^n = t^n, \quad n = 1, \dots, N \quad (8)$$

where the real value matrix  $g_r^n = [g_r^n(\mathbf{w}_n^n \cdot \bar{\beta}^n g_c^n + \mathbf{p}_n)]_{K \times P}$  is the output matrix of the second hidden layer. Thus, the desired weight vector, which connects the  $i$ th hidden node and the output layer nodes, could also be computed by

$$\hat{\alpha}^n = t^n g_r^{n\dagger} \quad (9)$$

where the complex matrix  $g_r^{n\dagger}$  is the Moore–Penrose generalized inverse of a complex matrix  $g_r^n$ .

### B. Assessment of the Training Cost

The node number of the hidden layers is set on the basis of the Hecht–Nelson method [53]: when the dimension of input data is  $n$ , the node number of the hidden layer is  $2n + 1$ . Thus, the node numbers of the first and second hidden layers are  $L = 2m + 1$  and  $S = 2F + 1$ , respectively, and the dimensions of  $\bar{\mathbf{w}}_c^n$ ,  $\mathbf{b}^n$ ,  $\bar{\beta}^n$ ,  $\bar{\mathbf{w}}_r^n$ ,  $\mathbf{p}^n$ , and  $\bar{\alpha}^n$  could be further written as  $(2m + 1) \times m$ ,  $(2m + 1) \times 1$ ,  $F \times (2m + 1)$ ,  $(2F + 1) \times F$ ,  $(2F + 1) \times 1$ , and  $F \times (2F + 1)$ . For the total  $N$  subsets, the dimensions of  $\bar{\mathbf{w}}_c$ ,  $\mathbf{b}$ ,  $\bar{\beta}$ ,  $\bar{\mathbf{w}}_r$ ,  $\mathbf{p}$ , and  $\bar{\alpha}$  could be written as  $[(2m + 1) \times N] \times m$ ,  $[(2m + 1) \times N] \times 1$ ,  $F \times [(2m + 1) \times N]$ ,  $[(2F + 1) \times N] \times F$ ,  $[(2F + 1) \times N] \times 1$ , and

$F \times [(2F + 1) \times N]$ . Based on the ELM theory [50]–[53],  $\bar{\bar{\beta}}$  and  $\bar{\bar{\alpha}}$  are the tunable parameters, and their dimensions are  $F \times [(2m + 1) \times N]$  and  $F \times [(2F + 1) \times N]$ .

Meanwhile, for the full-join strategy, the dimensions of  $\bar{w}_c$ ,  $\bar{\beta}$ ,  $\bar{w}_r$ ,  $p$ , and  $\bar{\alpha}$  based on the Hecht–Nelson method are  $(2m + 1) \times m$ ,  $(2m + 1) \times 1$ ,  $(N \times F) \times (2m + 1)$ ,  $[2(N \times F) + 1] \times (N \times F)$ ,  $[2(N \times F) + 1] \times 1$ , and  $(N \times F) \times [2(N \times F) + 1]$ , respectively. Thus, comparing the traditional full-join strategy and the semijoin strategy, the dimensions of  $\bar{\beta}$  are the same; however, the dimension of  $\bar{\alpha}$  based on the semijoin strategy is  $(2F + 1) / (2N \times F + 1)$  of the ones based on the traditional full-join strategy, which could be obtained with the calculation of  $\{F \times [(2F + 1) \times N]\} / \{(N \times F) \times [2(N \times F) + 1]\}$ . Furthermore,  $(2F + 1) / (2N \times F + 1)$  will be less than 1 if  $N$  is larger than 1. Thus, it could be proven that the training burden based on the semijoin strategy is less than the ones based on the traditional full-join strategy even though there are  $N$  submodels in SJ-ELM.

Meanwhile, one should note that the submodels are independent of each other, so there does not exist any information interchange between submodels. Thus, the imaging process for a submodel with the output dimensions of  $(N_1 \times N_2 \times N_3) / N_{\max} \times 1$  could be regarded as a 2-D imaging problem with respect to the output dimensions and structure since the output of each submodel is a 2-D slice of the imaging domain along the direction of dimension  $N_{\max}$ , where  $N_{\max}$  is the maximum value of  $N_1$ ,  $N_2$ , and  $N_3$ . In other words, the proposed SJ-ELM divides the 3-D imaging problem into  $N_{\max}$  sets of 2-D imaging slices, and the output of each submodel is the corresponding slice of the 3-D imaging domain. Thus, different from other full-join methods that require a large number of training samples, the proposed model could solve the 3-D imaging problem with the cost of 2-D problems. Meanwhile, one should note that ELM randomly chooses hidden nodes and analytically determines the output weights for hidden layers of feedforward neural networks, which has much lower training costs than the traditional feedforward neural networks. Here, “random” means that the elements in the weight matrices are randomly generated instead of being obtained in the training. This is the merit of the ELM. The training cost is low since we only need to solve the matrices  $\bar{\alpha}$  and  $\bar{\beta}$ .

Furthermore, with the dimensions of the output layer increasing, which will lead to stronger nonlinearity, the node number of both hidden layers and/or the number of training samples should also be largely increased to converge. Thus, the dimensions of  $\bar{\beta}$  and  $\bar{\alpha}$  in the full-join strategy are much larger than them in the semijoin strategy, which means the heavier computational burden and more difficult convergence in training. Therefore, comparing with the full-join strategy, the semijoin strategy is more economical for the 3-D MWI problem. However, one should note that more CPU time will be needed to train the several submodels in parallel.

### C. Performance Evaluation

To prove the efficiency of SJ-ELM, we have added a performance evaluation to test the proposed SJ-ELM. Two

approximation problems in the complex domain used in [54] are employed to test the efficiency of the proposed model, and the fully complex extreme learning machine (CELM) [55] is selected as the comparison model. As given in the setting in [56], 10 000 training samples and 1000 testing samples are randomly drawn from the interval  $[0 + j0, 1 + j]$ . The first verification is based on a nonanalytic function, as shown in the following equation:

$$f(z) = f(x + jy) = e^{jy}(1 - x^2 - y^2) \quad (10)$$

and the second one is an analytic function given as

$$\begin{aligned} f(z) &= f(x + jy) \\ &= \sin(x) \cosh(y) + j \cos(x) \sinh(y). \end{aligned} \quad (11)$$

Considering the MWI problem that maps the scattered field data to the permittivity and/or the conductivity of objects, we modify the following function to map the complex domain to the real domain as:

$$f(z) = f(x + jy) = |e^{jy}(1 - x^2 - y^2)| \quad (12)$$

$$\begin{aligned} f(z) &= f(x + jy) \\ &= |\sin(x) \cosh(y) + j \cos(x) \sinh(y)| \end{aligned} \quad (13)$$

respectively, for (10) and (11).

Here, a performance index, i.e., the relative root-mean-squared error (RRMSE), is given as

$$\text{RRMSE} = \sqrt{\frac{\sum_{i=1}^N (y_i - \hat{y}_i)^2}{N}} / \sqrt{\frac{\sum_{i=1}^N (y_i)^2}{N}} \quad (14)$$

where  $y_i$  is the calculation result from (12) or (13) and  $\hat{y}_i$  is the corresponding output from the neural network. The average results of RRMSE and standard deviation (Dev) are shown in Table I. The calculations are performed on an Intel i7-9700 3.0-GHz machine with 64-GB RAM. Here, the node numbers of hidden layers are set as 50, 100, and 500, respectively, for CELM. The node number of both hidden layers from SJ-ELM is set to be the same value as the CELM. It could be seen that, compared with CELM, SJ-ELM has a more accurate and stable performance. Due to having two hidden layers in SJ-ELM, the running time is a little longer.

## IV. NUMERICAL RESULTS

In this section, three numerical examples are presented to verify the validity of the proposed SJ-ELM for MWI of 3-D objects. In the first example, the conventional VBIM is employed to compare and confirm the implementation efficiency and accuracy of SJ-ELM. The second example further compares the proposed model with VBIM to evaluate the super-resolution imaging ability of SJ-ELM. In the third example, the proposed model is evaluated by reconstructing the 3-D objects with high contrasts. All the inversions are performed on a workstation with 20-cores Xeon E2650 v3 2.3G CPU, 512-GB RAM. In the numerical examples, all the simulation settings, including excitation, receiving antennas, and boundary conditions, are the same in the forward models to generate the training and testing or synthetic “measured” data. Meanwhile, to avoid the “inverse crime,” the meshes

TABLE I  
PERFORMANCE COMPARISON OF CELM AND SJ-ELM

	Node number of hidden layer			CELM	SJ-ELM
Nonanalytic function	50	CPU time (s)	Training	1.3252	1.5548
		Testing	0.1654	0.1949	
		Training	RRMSE	0.0612	0.0097
		Dev		0.4826	0.0597
		Testing	RRMSE	0.0634	0.0114
		Dev		0.5103	0.0658
	100	CPU time (s)	Training	1.6952	1.8756
		Testing	0.2651	0.3215	
		Training	RRMSE	0.0564	0.0092
		Dev		0.4327	0.0462
		Testing	RRMSE	0.0587	0.0126
		Dev		0.4912	0.0487
	500	CPU time (s)	Training	2.1635	2.6352
		Testing	0.1654	0.1949	
		Training	RRMSE	0.0464	0.0083
		Dev		0.3621	0.0298
		Testing	RRMSE	0.0488	0.0096
		Dev		0.3916	0.0326
Analytic function	50	CPU time (s)	Training	1.2564	1.5485
		Testing	0.1649	0.1934	
		Training	RRMSE	0.0497	0.0132
		Dev		0.5931	0.1108
		Testing	RRMSE	0.0536	0.0151
		Dev		0.6318	0.1236
	100	CPU time (s)	Training	1.6752	1.8542
		Testing	0.2632	0.3187	
		Training	RRMSE	0.0461	0.0097
		Dev		0.4639	0.0312
		Testing	RRMSE	0.0494	0.0121
		Dev		0.4913	0.0367
	500	CPU time (s)	Training	2.2031	2.6217
		Testing	0.1713	0.2017	
		Training	RRMSE	0.0431	0.0089
		Dev		0.3854	0.0216
		Testing	RRMSE	0.0458	0.0094
		Dev		0.4133	0.0227

used in the forward modeling and inversion are different. The forward modeling mesh is smaller than that in the inversion, and they are not aligned. In fact, the forward modeling mesh can be curvilinear so that it captures the curved geometries, while the inversion mesh is the regular structured mesh with square elements, so there is a geometry approximation for curved objects.

#### A. EM Inversion Setups

In the three examples, the operating frequencies of are 300, 500, and 600 MHz, respectively. The corresponding wavelengths of the three examples are  $\lambda_0 = 1$  m,  $\lambda_0 = 0.6$  m, and  $\lambda_0 = 0.5$  m in the air, respectively.

For the first example, totally 98 transmitters are uniformly located in two  $2.4 \text{ m} \times 2.4 \text{ m}$  planes at  $z = -0.2$  m and  $z = 1.2$  m, respectively. The scattered fields are collected by a 128-receiver array uniformly located in two  $2.8 \text{ m} \times 2.8 \text{ m}$  planes at  $z = -0.1$  m and  $z = 1.1$  m, respectively. The imaging domain  $D$  enclosing the objects has the dimensions of  $0.8 \text{ m} \times 0.8 \text{ m} \times 0.8 \text{ m}$  and is discretized into  $40 \times 40 \times 40$  voxels with its center at  $(0, 0, 0.5)$  m.

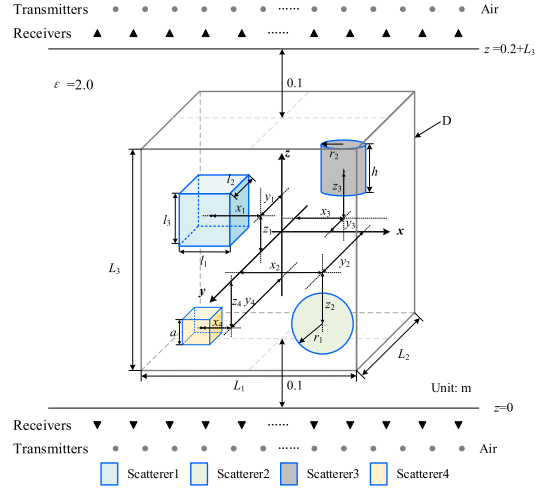


Fig. 2. 3-D training model for the first and second examples, where a cuboid, a cube, a sphere, and a cylinder as four nonoverlapping scatterers in DOI are employed to train SJ-ELM, and the parameters of these scatterers are assigned random values with the ranges shown in Table II. The transmitters and receivers are uniformly located in two planes on the upper and lower sides.

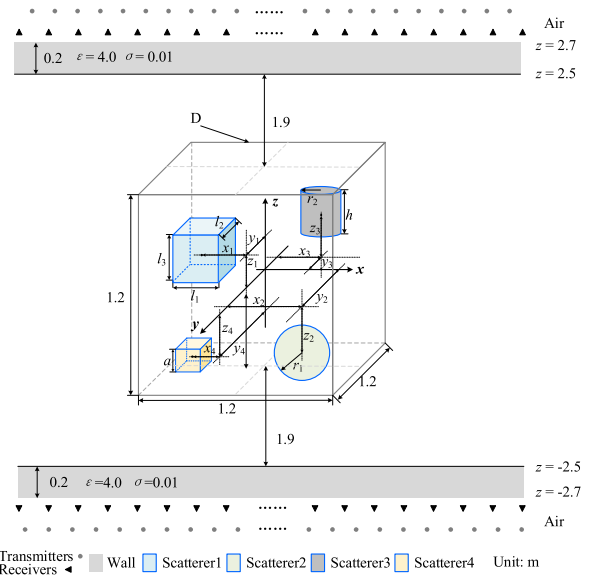


Fig. 3. 3-D training model for through-wall imaging as the third example where a cuboid, a cube, a sphere, and a cylinder as four nonoverlapping scatterers in DOI are employed to train SJ-ELM, and the parameters of these scatterers are assigned random values with the ranges shown in Table II. The transmitters and receivers are uniformly located in two planes on the upper and lower sides.

The input of this example is the vector of scattered field, and each vector contains 98 (transmitters)  $\times$  128 (receivers) elements. The corresponding outputs of the two channels are the vectors of distribution of the relative permittivity and conductivity, respectively, and the vector has the dimension of  $(40 \times 40 \times 40) \times 1$ . Based on the semijoin strategy, the output is discretized into 40 subsets.

The inversion domain  $D$  of the second example is with the dimensions of  $1.4 \text{ m} \times 1.4 \text{ m} \times 0.4 \text{ m}$ . The inversion domain  $D$  here is discretized into  $70 \times 70 \times 20$  voxels with its center at  $(0, 0, 0.3)$  m. Totally 128 transmitters are uniformly

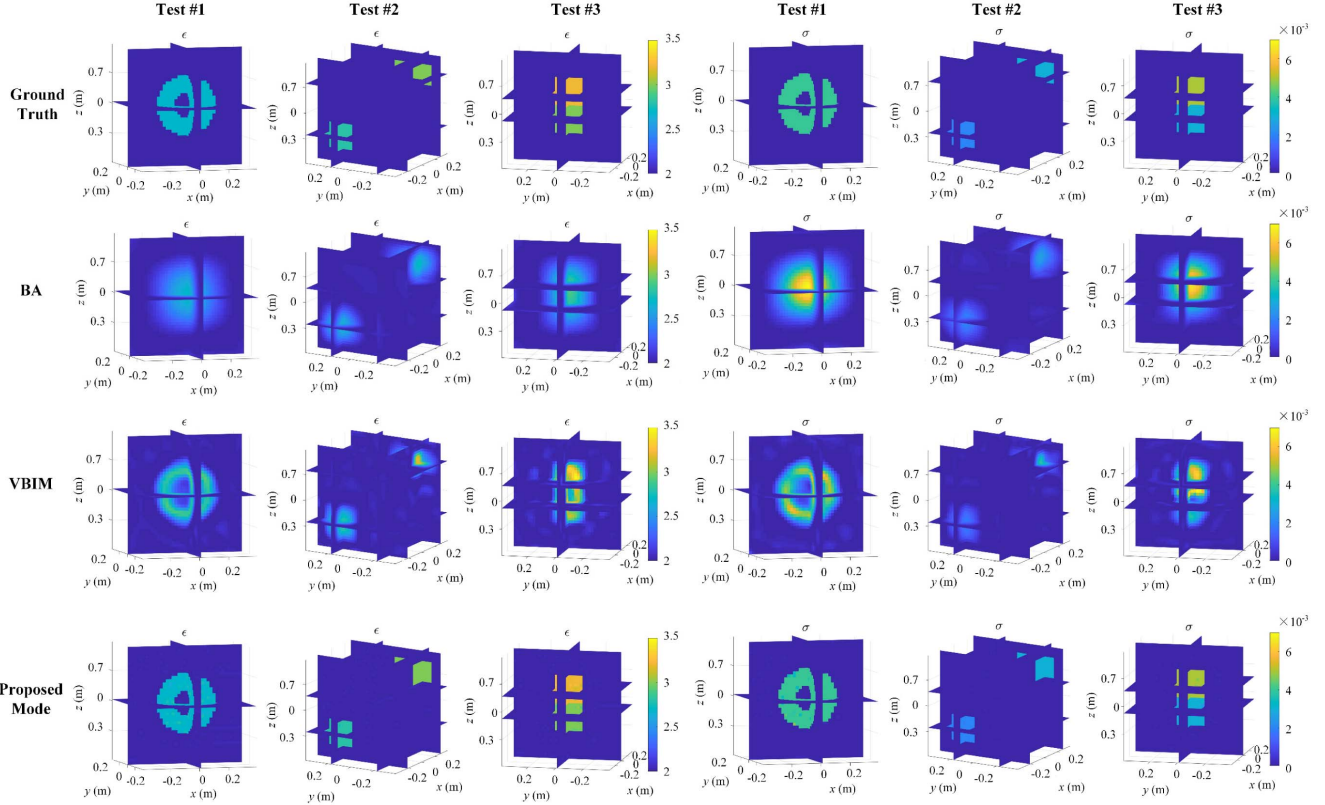


Fig. 4. Three different tests are used to evaluate the proposed SJ-ELM scheme. The first row is the ground truth, and from the second row to the fourth row, the imaging results from BA, VBIM, and the proposed model are shown, respectively. The first, second, and third columns show the distribution of relative permittivity, and the fourth, fifth, and sixth columns show the distribution of conductivity.

located in two  $2.8 \text{ m} \times 2.8 \text{ m}$  planes at  $z = -0.1 \text{ m}$  and  $z = 0.7 \text{ m}$ , respectively, and 162 receivers arrays uniformly located in two  $3.2 \text{ m} \times 3.2 \text{ m}$  planes at  $z = -0.2 \text{ m}$  and  $z = 0.8 \text{ m}$ , respectively. The imaging scenes, as shown in Fig. 2, of the first and second examples are similar. The input of this example is the vector of scattered field, and each vector contains 128 (transmitters)  $\times$  162 (receivers) elements. The outputs of the two channels are the vectors of distribution of the relative permittivity and conductivity, respectively, and the vector is with the dimension of  $(70 \times 70 \times 20) \times 1$ . Based on the semijoin strategy, the output is discretized into 70 subsets.

For the third example, another through-wall imaging circumstance, as shown in Fig. 3, is considered to evaluate the proposed model. The center of inversion domain  $D$  of is at  $(0, 0, 0)$  m and has the dimensions of  $1.2 \text{ m} \times 1.2 \text{ m} \times 1.2 \text{ m}$ . Here, the inversion domain  $D$  is discretized into  $60 \times 60 \times 60$  voxels. One hundred sixty-two transmitters are uniformly located in two  $2 \text{ m} \times 2 \text{ m}$  planes at  $z = -2.8 \text{ m}$  and  $z = 2.8 \text{ m}$ , respectively. Meanwhile, the scattered fields are collected by a 242-receiver array uniformly located in two  $2.5 \text{ m} \times 2.5 \text{ m}$  planes at  $z = -2.9 \text{ m}$  and  $z = 2.9 \text{ m}$ , respectively. Similar to the above two examples, the input of this example is the vector of scattered field, and each vector contains 162 (transmitters)  $\times$  242 (receivers) elements. The outputs of the two channels are the vectors of distribution of the relative permittivity and conductivity, respectively, and

the vector has the dimension of  $(60 \times 60 \times 60) \times 1$ . Based on the semijoin strategy, the output is discretized into 60 subsets.

In order to quantitatively evaluate the reconstruction performance, we define the model misfit and data misfit under the  $L_2$  norm as

$$\text{Err}_{\text{model}} = \frac{\|\mathbf{md}_R - \mathbf{md}_T\|}{\|\mathbf{md}_T\|} \quad (15)$$

$$\text{Err}_{\text{data}} = \frac{\|\mathbf{da}_R - \mathbf{da}_T\|}{\|\mathbf{da}_T\|} \quad (16)$$

where  $\mathbf{md}_T$  and  $\mathbf{md}_R$  are the true complex permittivity values of the model and the reconstructed complex permittivity values of the model for all the voxels, respectively.  $\mathbf{da}_T$  and  $\mathbf{da}_R$  are the vectors of measured scattered field data collected at all the receivers and the reconstructed scattered field, respectively.

#### B. Training Details for Three Examples

In these three numerical examples, we use a cuboid, a cube, a sphere, and a cylinder as four nonoverlapping scatterers in DOI to train SJ-ELM. As shown in Figs. 2 and 3, the centers of the cuboid, sphere cylinder, and cube, i.e.,  $x_1, y_1, z_1, x_2, y_2, z_2, x_3, y_3, z_3, x_4, y_4$ , and  $z_4$ , the side lengths of cuboid and cube, i.e.,  $l_1, l_2, l_3$ , and  $a$ , the radii of sphere and cylinder, i.e.,  $r_1$  and  $r_2$ , and the height of the cylinder, i.e.,  $h$ , are the variables and assigned random values with the ranges shown in Table II. The relative permittivities and conductivities of four scatterers are randomly set with different values in the

TABLE II  
PARAMETER RANGES FOR THE OBJECTS SHOWN IN FIGS. 2 AND 3 FOR EXAMPLES 1–3

		$x_1$	$y_1$	$z_1$	$x_2$	$y_2$	$z_2$	$x_3$	$y_3$	$z_3$	$x_4$	$y_4$	$z_4$	$l_1$	$l_2$
Example 1	Minimum	-0.3	-0.3	0.2	-0.3	-0.3	0.2	-0.3	-0.3	0.2	-0.3	-0.3	0.2	0.02	0.02
	Maximum	0.3	0.3	0.8	0.3	0.3	0.8	0.3	0.3	0.8	0.3	0.3	0.8	0.2	0.2
Example 2	Minimum	-0.6	-0.6	0.2	-0.6	-0.6	0.2	-0.6	-0.6	0.2	-0.6	-0.6	0.2	0.02	0.02
	Maximum	-0.6	-0.6	0.4	-0.6	-0.6	0.4	-0.6	-0.6	0.4	-0.6	-0.6	0.4	0.1	0.1
Example 3	Minimum	-0.5	-0.5	-0.5	-0.5	-0.5	-0.5	-0.5	-0.5	-0.5	-0.5	-0.5	-0.5	0.02	0.02
	Maximum	0.5	0.5	0.5	0.5	0.5	0.5	0.5	0.5	0.5	0.5	0.5	0.5	0.4	0.4
		$l_3$	$a$	$r_1$	$r_2$	$h$	$\varepsilon_1$	$\sigma_1$	$\varepsilon_2$	$\sigma_2$	$\varepsilon_3$	$\sigma_3$	$\varepsilon_4$	$\sigma_4$	
Example 1	Minimum	0.02	0.02	0.02	0.02	0.02	2	0	2	0	2	0	2	2	0
	Maximum	0.2	0.2	0.2	0.2	0.2	4	0.01	4	0.01	4	0.01	4	0.01	0.01
Example 2	Minimum	0.02	0.02	0.02	0.02	0.02	2	0	2	0	2	0	2	2	0
	Maximum	0.1	0.1	0.1	0.1	0.1	5	0.03	5	0.03	5	0.03	5	0.03	0.03
Example 3	Minimum	0.02	0.02	0.02	0.02	0.02	1	0	1	0	1	0	1	0	
	Maximum	0.4	0.4	0.4	0.4	0.4	7	0.08	7	0.08	7	0.08	7	0.08	

Remark: the unit of length is meter.  $\varepsilon_i$  and  $\sigma_i$  are the relative permittivity and conductivity value of  $i$ th object, respectively.

TABLE III  
MODEL MISFITS AND DATA MISFITS OF BA, VBIM, AND THE PROPOSED MODEL FOR TESTS #1–3

	Model misfit (%)		
	BA	VBIM	Proposed model
Test #1	23.259	10.352	3.656
Test #2	30.231	13.346	3.764
Test #3	29.245	12.622	3.811
	Data misfit (%)		
	BA	VBIM	Proposed model
Test #1	17.322	0.725	2.517
Test #2	11.019	1.074	5.003
Test #3	18.254	0.985	4.156

range of [2, 4] and [0, 0.01] for the first examples, [2, 5] and [0, 0.03] for the second example, and [1, 7] and [0, 0.08] for the third example. The proposed SJ-ELM is trained with totally 200 randomly generated training samples for the three examples, respectively. The node number of two hidden layers is set based on the Hecht–Nelson method [53]. One should note that SJ-ELM should be trained for these three examples, respectively, due to different imaging conditions. Meanwhile, all the parameters in the trained model are settled. When the scattered field data are input to the trained model, the corresponding output is unique.

### C. Comparisons With Conventional Inversion Methods

To evaluate the imaging accuracy and efficiency of the proposed SJ-ELM, its imaging results are compared with those from VBIM. As shown in Fig. 4, Test #1 has a single object, and Test #2 has two separated and different objects, while these two objects are tangent in Test #3. For Test #1, the radii of the outer and inner circles are 0.2 and 0.1 m ( $0.2\lambda$  and  $0.1\lambda$ ). For Test #2, the upper cuboid has the dimensions of  $0.3 \text{ m} \times 0.2 \text{ m} \times 0.2 \text{ m}$  ( $0.3\lambda \times 0.2\lambda \times 0.2\lambda$ ), and the other cuboid has the dimensions of  $0.2 \text{ m} \times 0.2 \text{ m} \times 0.2 \text{ m}$  ( $0.2\lambda \times 0.2\lambda \times 0.2\lambda$ ). For Test #3, the cuboid has the dimensions of  $0.2 \text{ m} \times 0.2 \text{ m} \times 0.4 \text{ m}$  ( $0.2\lambda \times 0.2\lambda \times 0.4\lambda$ ).

The contrasts of the three test samples are also gradually increased. As the contrast values increase and the geometric shape of objects becomes more complex, it is more and more difficult for VBIM to achieve a low data misfit and model

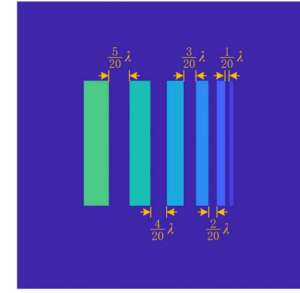


Fig. 5. Top view of Test #4. The distances between objects are  $5/20\lambda$ ,  $4/20\lambda$ ,  $3/20\lambda$ ,  $2/20\lambda$ , and  $1/20\lambda$ . Meanwhile, the relative permittivity and conductivity of these six objects are gradually decreased along the positive  $x$ -direction, i.e.,  $3.2\text{--}2.2$  with the step of  $-0.2$  for the relative permittivity and  $0.012\text{--}0.002$  with the step of  $-0.002$  for conductivity.

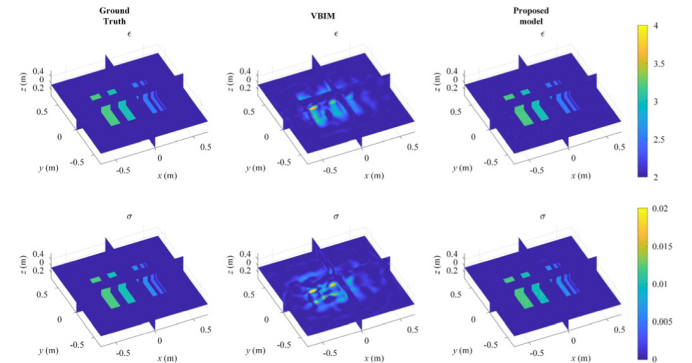


Fig. 6. Test #4 is employed to evaluate the super-resolution imaging ability of the proposed scheme. The first column shows the ground truth of the relative permittivity and conductivity, respectively. The second and third columns are the imaging results of the relative permittivity and conductivity from VBIM and the proposed scheme, respectively.

misfit, which could be revealed in Table III. In addition, one should note that the model misfits of VBIM are fluctuant for different test samples. On the contrary, the model misfits obtained from the proposed SJ-ELM model are always lower than VBIM, as shown in Table III.

Meanwhile, as shown in the fourth row of Fig. 4, the imaging results obtained from the proposed SJ-ELM are not

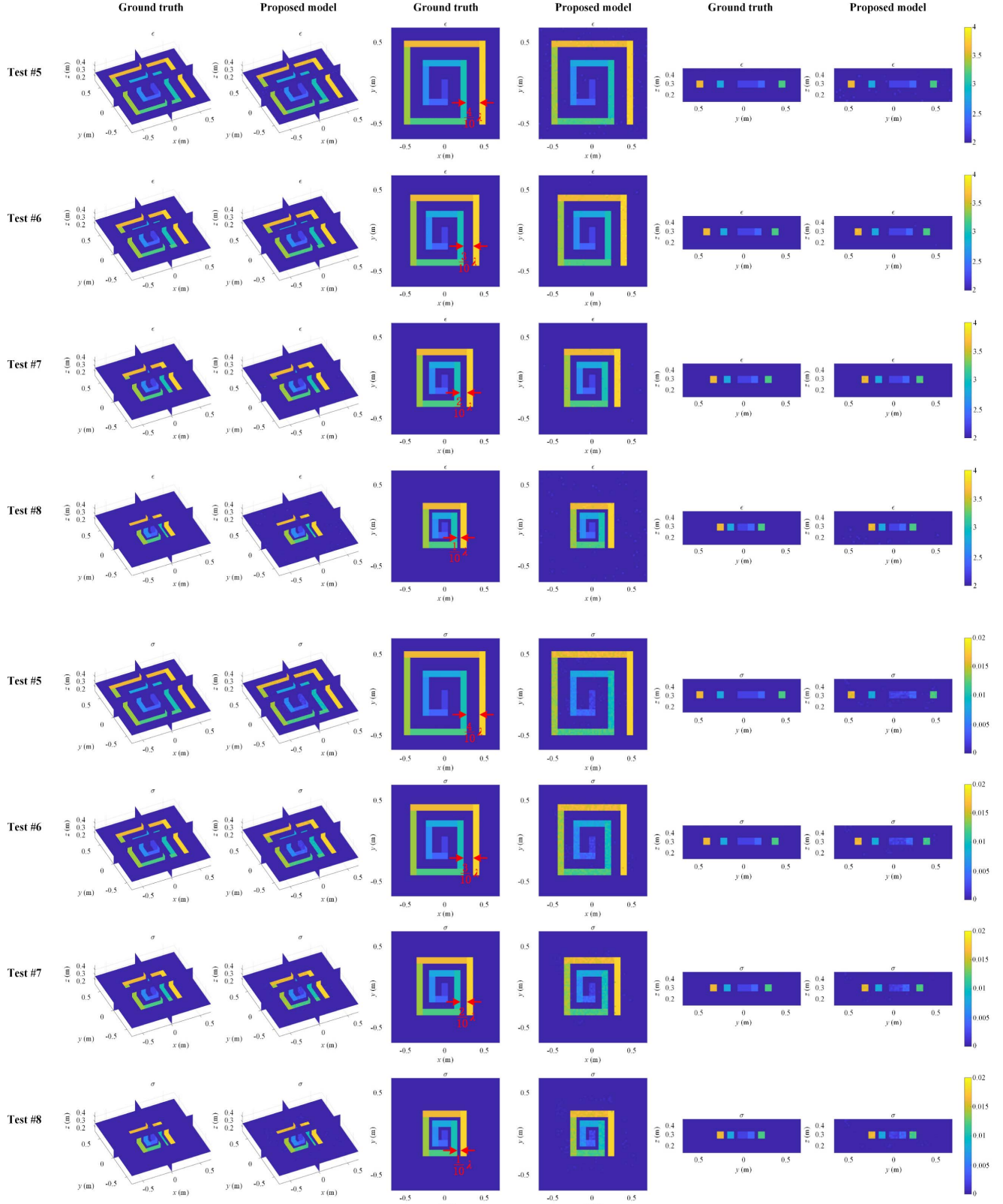


Fig. 7. Tests #5–8 are employed to further evaluate the super-resolution imaging ability of the proposed scheme. The first, third, and fifth columns are the 3-D perspective,  $xy$  slice at  $z = 0.3$  m, and  $yz$  slice at  $x = 0$  m of ground truth, respectively. The second, fourth, and sixth columns are the 3-D perspective,  $xy$  slice at  $z = 0.3$  m, and  $yz$  slice at  $x = 0$  m of the imaging results from the proposed scheme.

affected by different contrast values, and geometric shapes of objects and the model misfits, as shown in Table III, obtained from the proposed model almost remain unchanged.

This illustrates that the proposed SJ-ELM is more stable and competent to deal with MWI compared with the conventional VBIM.

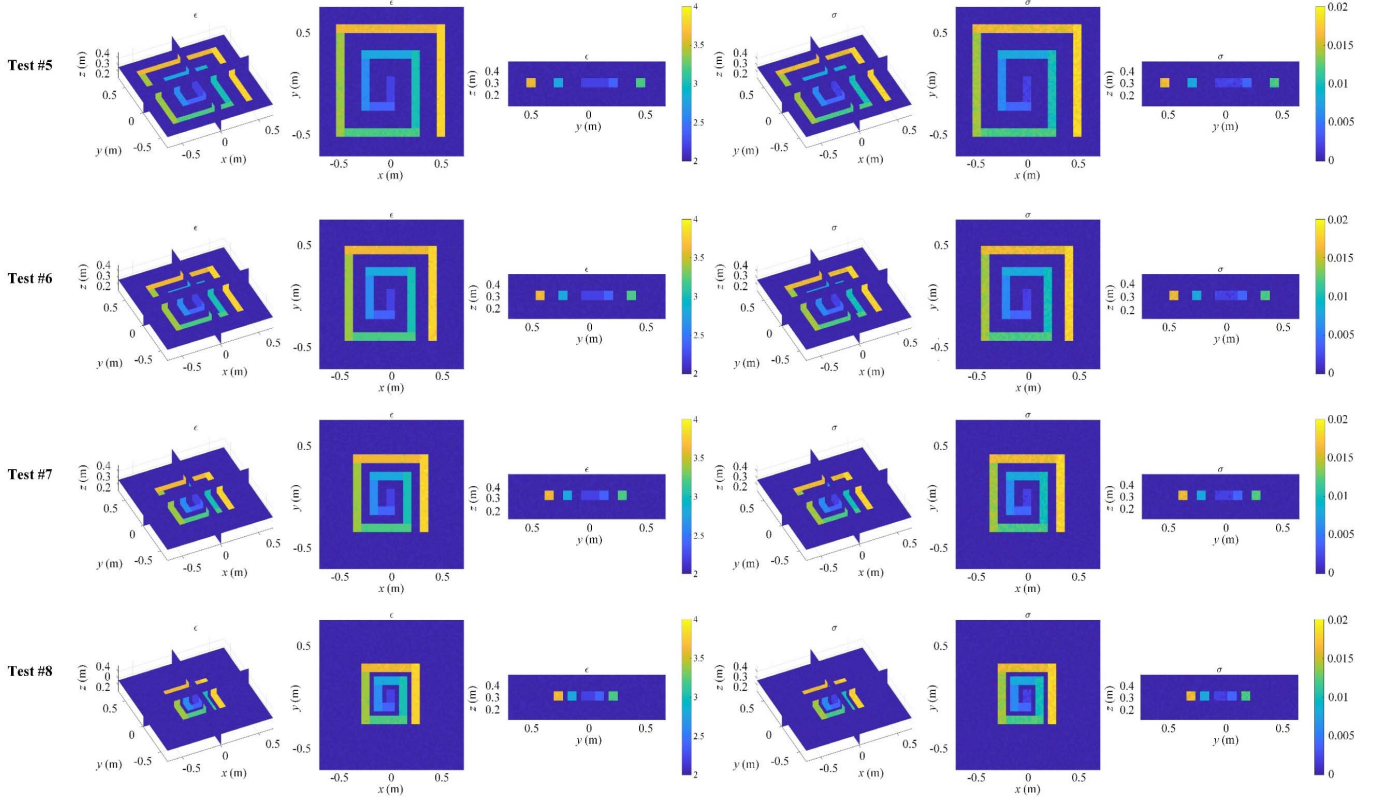


Fig. 8. First, second, and third columns are the 3-D perspective,  $xy$  slice at  $z = 0.3$  m, and  $yz$  slice at  $x = 0$  m of the relative permittivity imaging results from the proposed scheme in the 20-dB noise environment. The fourth, fifth, and sixth columns are the 3-D perspective,  $xy$  slice at  $z = 0.3$  m, and  $yz$  slice at  $x = 0$  m of the conductivity imaging results from the proposed scheme in the 20-dB noise environment.

Furthermore, as an example, each VBIM iteration takes about 40 min in Test #3; thus, the total time cost in Tests #1–3 of VBIM is much higher than that of the trained SJ-ELM which spends less than 1 s to accurately -D objects, even though about 1-h training time of SJ-ELM is added.

Thus, comparing with VBIM, the trained proposed SJ-ELM model can achieve more accurate and stable imaging performance and higher imaging efficiency.

Meanwhile, for the full-join strategy in this example, the dimensions of  $\bar{\beta}$  and  $\bar{\alpha}$  based on the Hecht–Nelson method are  $(40 \times 40 \times 40) \times (128 \times 98 \times 2 + 1)$  and  $(40 \times 40 \times 40) \times (40 \times 40 \times 40 \times 2 + 1)$ , i.e.,  $64\,000 \times 25\,089$  and  $64\,000 \times 128\,001$ , respectively. However, for the semijoin strategy with parallel training in this example, the dimensions of  $\bar{\beta}$  and  $\bar{\alpha}$  based on the Hecht–Nelson method are  $(40 \times 40) \times [(2 \times 128 \times 98 + 1) \times 40]$  and  $(40 \times 40) \times [(2 \times 40 \times 40 + 1) \times 40]$ , i.e.,  $1600 \times 1\,003\,560$  and  $1600 \times 128\,040$ . Thus, compared with the full-join strategy, which requires a heavy burden for the memory and will lead to an enormous challenge for computational efficiency, the proposed semijoin strategy is easier to converge and more suitable for the 3-D MWI problem. More proven details can be referred to Appendix B.

#### D. Super-Resolution Imaging

To test the super-resolution imaging ability of the proposed SJ-ELM, two parts are investigated. First, VBIM is employed

as a comparison model to evaluate the proposed model with Test #4. Then, we design a series of test cases to further evaluate the super-resolution imaging ability of the proposed SJ-ELM in noise-free and noisy environments, respectively. According to the definition in [57], as the image resolution is less than 0.25 wavelength, it can be called super-resolution. There are six objects in Test #4, as shown in Fig. 5, and the adjacent spacings between them are  $5/20\lambda$ ,  $4/20\lambda$ ,  $3/20\lambda$ ,  $2/20\lambda$ , and  $1/20\lambda$ , respectively; meanwhile, the relative permittivity and conductivity of them are gradually decreased, along the positive  $x$ -direction. The height of each object is 0.1 m (or  $0.167\lambda$ ).

Fig. 6 shows the imaging results of VBIM and the proposed model, respectively. It could be seen that the imaging results of VBIM cannot distinguish the fifth and sixth objects separately; however, the proposed model could clearly image both relative permittivity and conductivity of the objects. The imaging performance of VBIM and the proposed model also could be revealed with data misfits and model misfits, which are 1.12% and 11.534% for VBIM and 2.592% and 3.215% for the proposed model, respectively. Thus, compared with VBIM in terms of imaging resolution, the proposed model could have better performance and achieve super-resolution imaging results.

Then, to further evaluate the imaging resolution of the proposed model, we design a series of tests, as shown in Fig. 7, where the adjacent spacings between objects are gradually decreased to  $4/10\lambda$ ,  $3/10\lambda$ ,  $2/10\lambda$ , and  $1/10\lambda$  from Test #5 to

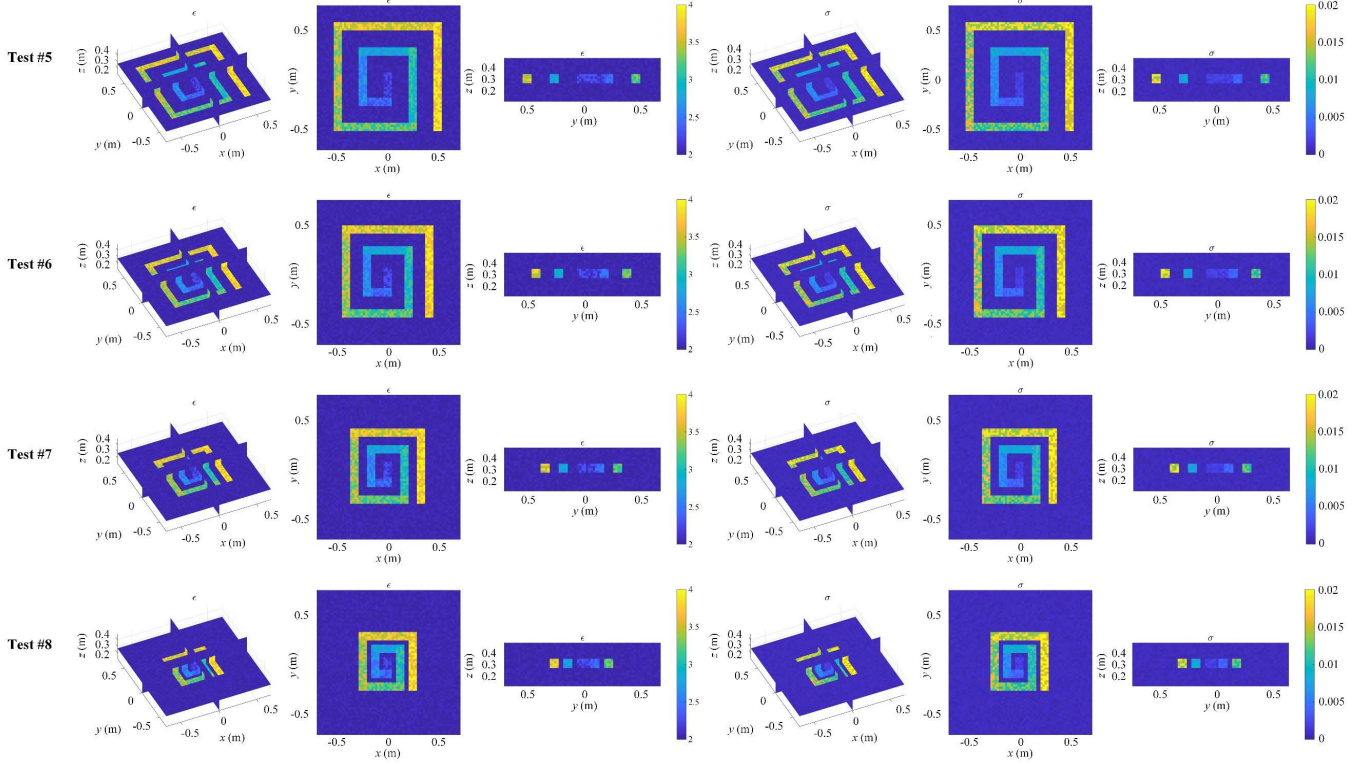


Fig. 9. First, second, and third columns are the 3-D perspective,  $xy$  slice at  $z = 0.3$  m, and  $yz$  slice at  $x = 0$  m of the relative permittivity imaging results from the proposed scheme in the 10-dB noise environment. The fourth, fifth, and sixth columns are the 3-D perspective,  $xy$  slice at  $z = 0.3$  m, and  $yz$  slice at  $x = 0$  m of the conductivity imaging results from the proposed scheme in the 10-dB noise environment.

Test #8, respectively. The height of each object is 0.1 m (or  $0.167\lambda$ ). Meanwhile, the relative permittivity and conductivity of nine connected objects are gradually increased from the inside to the outside, i.e., 2.2–3.8 with the step of 0.2 for the relative permittivity and 0.002–0.018 with the step of 0.002 for conductivity. For these test cases, it is very difficult for VBIM to obtain a low model misfit. The evaluated data misfits of VBIM are 0.716%, 0.712%, 0.705%, and 0.708% for Tests #5–8, respectively. Figs. 7–9 show the imaging results obtained from the proposed model in the noise-free, –20- and –10-dB Gaussian white noise environments (i.e., the signal-to-noise ratio (SNR) of power is infinity, 20 dB, and 10 dB, respectively). It could be seen the proposed model can image a stable imaging performance in the noise-free environment and have a stable trend of model misfits even though the distances between objects changed, and the corresponding model misfits are small, as shown in Table IV. The evaluated data misfits are 2.357%, 2.269%, 2.177%, and 2.634% for Tests #5–8, respectively, in the noise-free environment, also reveal the similar stable trend. Meanwhile, the boundary between two connected objects can be clearly imaged, which is a challenging task to image two connected objects with close relative permittivity and conductivity by other traditional methods. Meanwhile, as shown in Fig. 7, the  $xy$  slice at  $z = 0.3$  m and the  $yz$  slice at  $x = 0$  m present the reconstructed results in a transverse plane and along the longitudinal axis, respectively. However, the anisotropy of the resolution is not observed from these two slices. This may be due to the fact that our transmitter and receiver apertures are large enough to avoid obvious anisotropy

TABLE IV  
MODEL MISFITS OF THE PROPOSED SCHEME FOR TESTS #5–8 IN  
NOISE-FREE, 20-dB NOISE, AND 10-dB NOISE ENVIRONMENTS,  
RESPECTIVELY

		Noise-free	20 dB	10 dB
Model misfit	Test #5	3.585%	6.103%	16.703%
	Test #6	3.624%	6.232%	16.654%
	Test #7	3.611%	6.098%	16.695%
	Test #8	3.632%	6.112%	16.709%

in resolution. Then, as shown in Figs. 8 and 9, as the noise increases, the imaging results become more and more blurred; however, the outline of objects also can be distinguished, and the model misfits of four test cases, as shown in Table IV, almost remain the same levels for both 20- and 10-dB noise environments, although the distances between objects are closer. Thus, the proposed method has good antinoise ability and super-resolution imaging ability in the noisy environment.

#### E. High Contrast

As shown in Fig. 10, Test #9 consists of 27 spheres placed in three layers, and each layer has three spheres. The center position, radius, relative permittivity, and conductivity of each sphere are listed in Table V. The relative permittivity and conductivity of these spheres are gradually increased with the steps of 0.2 and 0.002 from 1.2 and 0.002, respectively. The radius of each sphere is  $0.32\lambda$ . Thus, the maxima of

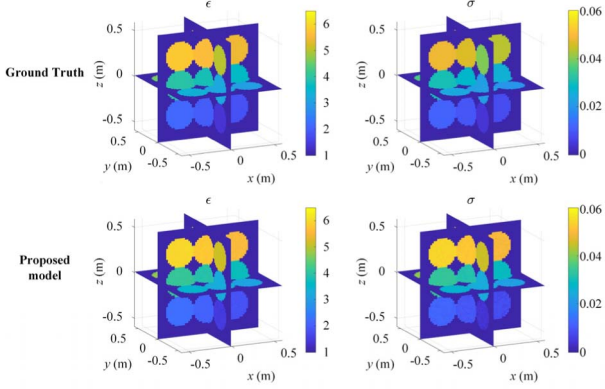


Fig. 10. Relative permittivity and conductivity imaging results of Test #9 from the proposed scheme, where imaging objects are with high contrast.

the relative permittivity and conductivity are 6.4 and 0.054, respectively.

Fig. 10 shows the 3-D imaging results from the proposed model. Meanwhile, we select three slices located at  $z = -0.32$  m,  $z = 0$  m, and  $z = -0.32$  m, as shown in Fig. 11, to illustrate the imaging results clearly. It can be seen that both the permittivity and conductivity imaging results obtained from the proposed model can distinguish a good spatial resolution and provide accurate estimates of the contrast permittivity imaging and conductivity imaging even though two adjacent spheres have close values of dielectric parameters, or the object has high contrast. The model misfit of this case is 3.88%, and the model misfits of relative permittivity and conductivity are 2.89% and 12.5%, respectively. The evaluated data misfit is 1.225%. However, for the conventional method, such as VBIM, it is really difficult to converge for this test, which consists of objects with high contrasts, but the proposed SJ-ELM can obtain super-resolution imaging results in the application of through-wall imaging.

Throughout the model misfits and data misfits, which are obtained from the proposed SJ-ELM, from the first numerical example to the third numerical example, the contrasts of objects are gradually increased, and the model misfits remain at the same level because the objective function of the machine learning method is based on the model misfit. However, with the relative permittivity increasing, the corresponding data misfits are gradually decreased. This is because with contrast increasing, the nonlinearity of the inversion problem is aggravated, and the caused multisolution problem brings more solutions to satisfy the desired data misfit. The machine learning method could reconstruct the objects well even though the objects are with high contrasts. Thus, with contrast increasing, the data misfit reveals a decreasing trend even though model misfits are at the same level. This is quite different from the conventional inverse methods, which still could have a very low data misfit when the objects are with high contrasts; however, the model misfit is also very large. Compared with conventional inverse methods, the advantage of the machine learning-based method is that a stable model misfit could be obtained even though the objects have high contrasts.

TABLE V  
PARAMETERS OF EACH SPHERE OF TEST #9

No.	Center position (m)			Radius (m)	Relative permittivity	Conductivity
	x	y	z			
1	-0.32	-0.32	-0.32	0.16	1.2	0.002
2	0	-0.32	-0.32	0.16	1.4	0.004
3	-0.32	0.32	-0.32	0.16	1.6	0.006
4	-0.32	0	-0.32	0.16	1.8	0.008
5	0	0	-0.32	0.16	2.0	0.010
6	0.32	0	-0.32	0.16	2.2	0.012
7	-0.32	0.32	-0.32	0.16	2.4	0.014
8	0	0.32	-0.32	0.16	2.6	0.016
9	0.32	0.32	-0.32	0.16	2.8	0.018
10	-0.32	-0.32	0	0.16	3.0	0.020
11	0	-0.32	0	0.16	3.2	0.022
12	-0.32	0.32	0	0.16	3.4	0.024
13	-0.32	0	0	0.16	3.6	0.026
14	0	0	0	0.16	3.8	0.028
15	0.32	0	0	0.16	4.0	0.030
16	-0.32	0.32	0	0.16	4.2	0.032
17	0	0.32	0	0.16	4.4	0.034
18	0.32	0.32	0	0.16	4.6	0.036
19	-0.32	-0.32	0.32	0.16	4.8	0.038
20	0	-0.32	0.32	0.16	5.0	0.040
21	-0.32	0.32	0.32	0.16	5.2	0.042
22	-0.32	0	0.32	0.16	5.4	0.044
23	0	0	0.32	0.16	5.6	0.046
24	0.32	0	0.32	0.16	5.8	0.048
25	-0.32	0.32	0.32	0.16	6.0	0.050
26	0	0.32	0.32	0.16	6.2	0.052
27	0.32	0.32	0.32	0.16	6.4	0.054

## V. EXPERIMENTAL DATA

To further evaluate the proposed model, the 3-D experimental data from the Fresnel database [58] are used in this test. Here, simulation data are used to train the model, and actual measured data are employed to test the trained model, where the simulation setting is the same as the experimental environment. A “CubeSpheres” target with copolarized data, as shown in Fig. 12, is adopted. Here, we select two frequency points at 3 and 8 GHz for the evaluation. Each sphere has a diameter of 15.9 mm and a relative permittivity of 2.6. They are assembled in order to create a cube of the side length of 47.6 mm. In the measurement environment, the transmitter arrays are located on a sphere with the radius of 1.796 m surrounding the target, where the azimuthal angle  $\theta_s$  is in the range from  $20^\circ$  to  $340^\circ$  with the step of  $40^\circ$ , and the polar angle  $\phi_s$  is in the range from  $30^\circ$  to  $150^\circ$  with the step of  $15^\circ$ . The receiver arrays are located on the azimuthal plane with the radius of 1.796 m, and the azimuthal angle  $\theta_r$  is in the range from  $0^\circ$  to  $350^\circ$  with the step of  $10^\circ$ . The experimental scattered data are corrected for drift errors and calibrated, successively [59].

According to the experimental setup, the cubic volume imaging domain of dimensions  $100 \times 100 \times 100$  mm<sup>3</sup>, centered at  $(0, 0, 0)$  of the coordinate system, is divided into  $96 \times 96 \times 96$  voxels. Based on the measurement environment and the experimental setup, totally 200 training samples with a frequency of 3 and 8 GHz are produced and employed to train the proposed model, respectively. Each training sample contains a cuboid, a cube, a sphere, and a cylinder as four

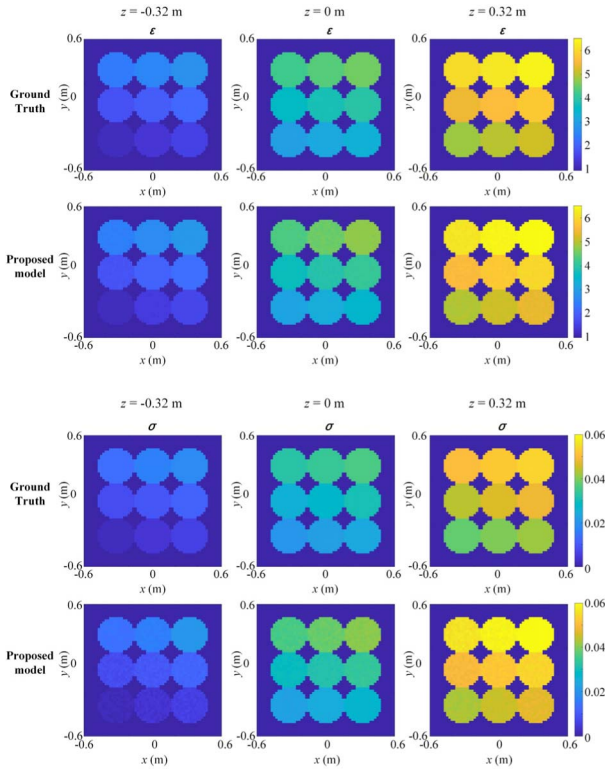


Fig. 11. Relative permittivity and conductivity imaging results of  $xy$  slices at  $z = -0.32, 0$ , and  $0.32$  from the proposed scheme, respectively, where the relative permittivity and conductivity of each slice are gradually increased, and the model misfit of this case is  $3.88\%$ , and the model misfits of relative permittivity and conductivity are  $2.89\%$  and  $12.5\%$ , respectively.

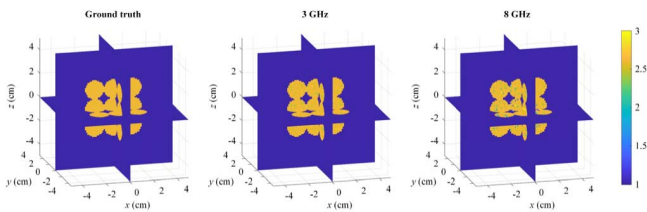


Fig. 12. Ground-truth and imaging results of relative permittivity profiles of “CubeSphere” at 3 and 8 GHz by the proposed scheme, respectively.

nonoverlapping scatterers in DOI, which are chosen similar to those in Section IV. The relative permittivities of four scatterers are randomly set with different values in the range of [1, 4]. The measured scattered field data at 3 and 8 GHz of the “CubeSpheres” target are employed as the input of the test, and the reconstructed relative permittivity distribution of both frequency points from the proposed model is obtained, as shown in Fig. 12. The model misfits of the reconstructed targets at 3 and 8 GHz are  $4.533\%$  and  $5.236\%$ , respectively. Meanwhile, the data misfits for the reconstructed targets at 3 and 8 GHz are  $4.692\%$  and  $6.132\%$ , respectively. Because the nonlinearity at 8 GHz is stronger than that at 3 GHz, with the same number of the receiver arrays, the imaging errors, model misfit, and data misfit at 8 GHz are higher than those at 3 GHz. The results from the experimental data further verify the validity of the proposed model, which has a good

performance in the practical experimental environment for the MWI problems.

## VI. CONCLUSION

MWI, which is a noninvasive and nondestructive technique to inspect materials by using incident electromagnetic waves generated in the microwave range, has gained a lot of interest recently. Due to the intrinsic nonlinearity of the inverse scattering problem and the ill-posedness of the discretized matrix equations, it is a challenging task to find a reliable, accurate, and numerically efficient inversion method. The combination of wave physics with machine learning techniques is a novel direction to study MWI problems.

In this article, an SJ-ELM model is proposed for super-resolution 3-D quantitative imaging of objects with high contrasts. In the proposed SJ-ELM, two channels convert the complex-valued scattered field data to the real permittivity and conductivity values of the imaging domain, respectively. Each channel is constructed with a shallow neural network structure based on the semijoin strategy. The semijoin strategy can decrease the inner matrix dimensions and improve the convergence performance of the model in the performance of super-resolution imaging, so it is employed to connect between the nodes of hidden layers and output layer to realize super-resolution imaging.

The proposed SJ-ELM is evaluated by both synthetic data and experimental data measured in the laboratory, respectively. Through comparison with a conventional method, e.g., VBIM, the proposed SJ-ELM model can achieve more accurate and stable imaging performance and higher imaging efficiency. In terms of imaging resolution, the proposed model can have better performance and achieve super-resolution imaging results. Meanwhile, in a noisy environment, the proposed method also shows good antinoise ability and super-resolution imaging ability, even when the measured data are contaminated by  $-10$ -dB noise. In addition, in the application of through-wall imaging, the proposed SJ-ELM can obtain super-resolution imaging results, even when the objects are with high contrasts that are really difficult for a conventional method, such as VBIM to converge. Finally, the reconstruction of the laboratory-measured scattered field data at 3 and 8 GHz for “CubeSphere” provided by Institute Fresnel demonstrates the adaptability of the proposed SJ-ELM for high-frequency experimental data.

## APPENDIX A

The determination of  $N$  is very interesting. To reach the super-resolution 3-D imaging, the imaging domain is divided into a huge number of voxels, which means a heavy computational burden and difficult convergence in training. Thus, we try to reduce the computational burden and the training cost for the super-resolution imaging, and a new semijoin strategy is proposed to divide the output matrix into  $N$  subsets. As mentioned above, if  $N$  is larger than 1, the ratio  $(2F + 1)/(2N \times F + 1)$ , which is between that of  $\bar{\alpha}$  based on the semijoin strategy and the traditional full-join strategy, will be less than 1. Based on the relationship of  $(2F + 1)$

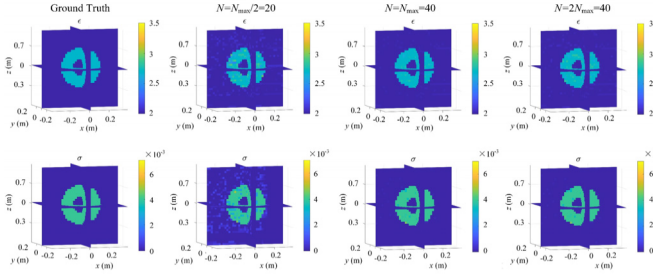


Fig. 13. Comparison of imaging performance between different values for  $N$ . The first row shows the distribution of the relative permittivity, and the second row shows the distribution of the conductivity.

TABLE VI  
MODEL MISFITS BETWEEN DIFFERENT VALUES FOR  $N$

Value of $N$	20	40	80
Model misfit (%)	6.367	3.656	3.328

$/(2N \times F + 1)$ , the ratio value will decrease with the increase in  $N$ . Thus, with the increase in  $N$ , the training burden will be decreased. However, as the reviewer said, if  $N$  is a very large number, resulting in each image having small memory, there will be a huge number of subimages to model. It is hard to quantitatively determine  $N$  to reach a balance between the training burden and the number of submodels for different application environments. Thus, we employ a trial-and-error approach to determine the value of  $N$  for different examples. Take the first numerical example as an example, we define  $N_{\max}$  as the maximum value of  $N_1$ ,  $N_2$ , and  $N_3$ ; then,  $N$  is set equal to  $N_{\max}/2$ ,  $N_{\max}$ , and  $2N_{\max}$ , i.e., 20, 40, and 80, for training, respectively.

The imaging results of different  $N$  values are shown in Fig. 13, and the corresponding model misfits are also provided in Table VI. It could be seen that, when  $N$  equals 20, the obtained model misfit is higher than other values of  $N$ . However, when the value of  $N$  is increased to 80 from 40, the model misfits of both  $N$  values are at the same level even though the model misfit based on  $N$  value with 80 is decreased slightly. As expected, if  $N$  is a very large number, there will be a huge number of subimages to model. Thus,  $N$  is recommended to set with the maximum value of  $N_1$ ,  $N_2$ , and  $N_3$ . Therefore, in our article,  $N$  is set with the value of 40, 70, 60, and 96 for the three examples and experimental data, respectively.

## APPENDIX B

A full-join strategy-based modeling method, i.e., dual-module NMM-image enhancing module (IEM) machine learning scheme, in [44] is employed as a comparison model here to evaluate the efficiency of the proposed method in this article. We select the first numerical example in this article as an example. The specific description of this numerical example is described in the text. Both SJ-ELM, where  $N$  is set to 40, and NMM-IEM are trained with totally 200 randomly generated training samples. The node numbers of hidden layers

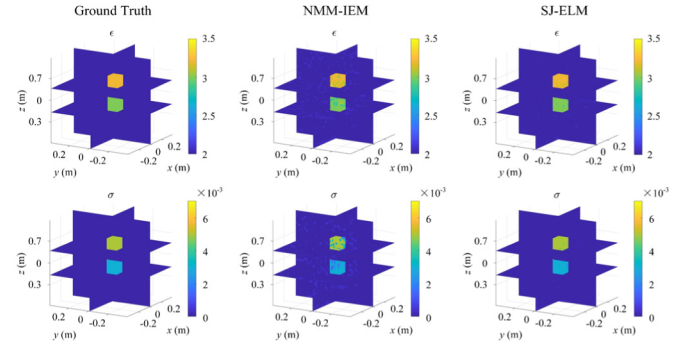


Fig. 14. Comparison of imaging performance between NMM-IEM and SJ-ELM. The first row shows the distribution of the relative permittivity, and the second row shows the distribution of the conductivity.

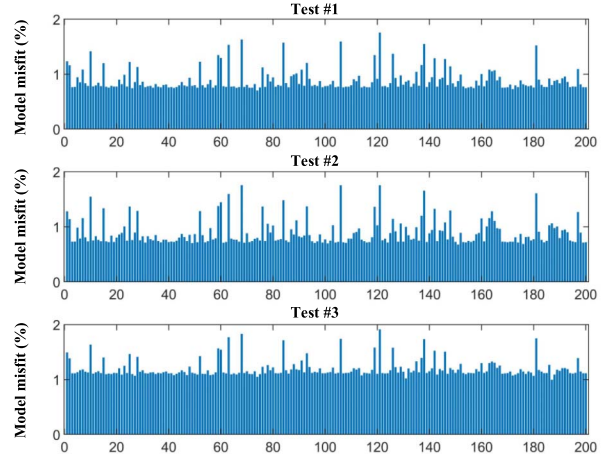


Fig. 15. Model misfits of relative permittivity between three test samples used in this article and 200 training samples.

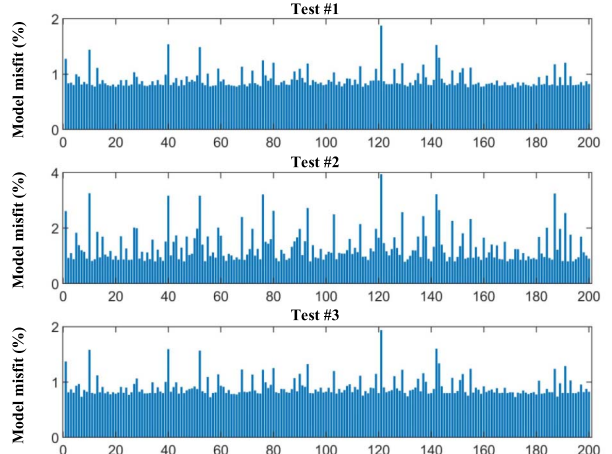


Fig. 16. Model misfits of conductivity between seven test samples used in this article and 200 training samples.

from both methods are set on the basis of the Hecht–Nelson method [53]. Test #3 is selected as the testing sample.

On the one hand, from the imaging results shown in Fig. 14, it could be seen that the imaging performance of SJ-ELM is better than NMM-IEM, where the background is clearer,

and the parameter distributions, including relative permittivity and conductivity, of two scatterers are more accurate. The model misfits of NMM-IEM and SJ-ELM also confirm the imaging performance of both methods, where 8.682% for NMM-IEM and 3.811% for SJ-ELM. For the full-join strategy-based NMM-IEM in this example, the dimensions of  $\bar{\beta}$  and  $\bar{\alpha}$  based on the Hecht–Nelson method are  $(40 \times 40 \times 40) \times (128 \times 98 \times 2 + 1)$  and  $(40 \times 40 \times 40) \times (40 \times 40 \times 40 \times 2 + 1)$ , respectively. For the semijoin strategy-based SJ-ELM with parallel training in this example, the dimensions of  $\bar{\beta}$  and  $\bar{\alpha}$  based on the Hecht–Nelson method are  $(40 \times 40) \times [(2 \times 128 \times 98 + 1) \times 40]$  and  $(40 \times 40) \times [(2 \times 40 \times 40 + 1) \times 40]$ , i.e.,  $1600 \times 1003560$  and  $1600 \times 128040$ . The numbers of unknowns for NMM-IEM and SJ-ELM are  $1605\,696\,000 + 8\,192\,064\,000 = 9\,797\,760\,000$  and  $1605\,696\,000 + 204\,864\,000 = 1\,810\,560\,000$ , respectively, where the number of unknowns of SJ-ELM is significantly smaller than the number of unknowns of NMM-IEM. Thus, compared with full-join strategy-based NMM-IEM, SJ-ELM is much easier to converge and can obtain better imaging performance.

On the other hand, in the calculation process, NMM-IEM requires 85.55-GB memory, and SJ-ELM requires 30.27-GB memory in solving  $\bar{\beta}$  and  $\bar{\alpha}$ . Thus, for the 3-D super-resolution imaging problem, NMM-IEM that requires an unacceptable burden for computer memory will lead to an enormous challenge for computational efficiency.

## APPENDIX C

To ensure the generalization ability of the proposed model, we take the first example in this article as an example. The model misfits between the three test cases and 200 training samples are shown in Figs. 15 and 16, for the relative permittivity and conductivity, respectively. It could be seen that the test cases and training samples have large model misfits. Meanwhile, from Table II in this article, the imaging results obtained from the proposed SJ-ELM are not affected by different contrast values, and geometric shapes of objects and the model misfits obtained from the proposed model almost remain unchanged. Thus, it could be concluded that the proposed model has good generalization ability even though the test sample is different from the training samples.

## REFERENCES

- [1] P.-H. Tournier *et al.*, “Numerical modeling and high-speed parallel computing: New perspectives on tomographic microwave imaging for brain stroke detection and monitoring,” *IEEE Trans. Antennas Propag. Mag.*, vol. 59, no. 5, pp. 98–110, Oct. 2017.
- [2] L. M. Neira, B. D. Van Veen, and S. C. Hagness, “High-resolution microwave breast imaging using a 3-D inverse scattering algorithm with a variable-strength spatial prior constraint,” *IEEE Trans. Antennas Propag.*, vol. 65, no. 11, pp. 6002–6014, Nov. 2017.
- [3] Q. H. Liu *et al.*, “Active microwave imaging. I. 2-D forward and inverse scattering methods,” *IEEE Trans. Microw. Theory Techn.*, vol. 50, no. 1, pp. 123–133, Jan. 2002.
- [4] C. Yu *et al.*, “Active microwave imaging II: 3-D system prototype and image reconstruction from experimental data,” *IEEE Trans. Microw. Theory Techn.*, vol. 56, no. 4, pp. 991–1000, Apr. 2008.
- [5] Z. Q. Zhang and Q. H. Liu, “Three-dimensional nonlinear image reconstruction for microwave biomedical imaging,” *IEEE Trans. Biomed. Eng.*, vol. 51, no. 3, pp. 123–133, Mar. 2004.
- [6] N. K. Nikolova, “Microwave imaging for breast cancer,” *IEEE Microw. Mag.*, vol. 12, no. 7, pp. 78–94, Dec. 2011.
- [7] R. Scapaticci, I. Catapano, and L. Crocco, “Wavelet-based adaptive multiresolution inversion for quantitative microwave imaging of breast tissues,” *IEEE Trans. Antennas Propag.*, vol. 60, no. 8, pp. 3717–3726, Aug. 2012.
- [8] M. T. Ghasr, M. J. Horst, M. R. Dvorsky, and R. Zoughi, “Wideband microwave camera for real-time 3-D imaging,” *IEEE Trans. Antennas Propag.*, vol. 65, no. 1, pp. 258–268, Jan. 2017.
- [9] G. Li and R. J. Burkholder, “Hybrid matching pursuit for distributed through-wall radar imaging,” *IEEE Trans. Antennas Propag.*, vol. 63, no. 4, pp. 1701–1711, Apr. 2015.
- [10] I. Catapano, L. Crocco, L. Di Donato, and T. Isernia, “Advances in inverse scattering arising from the physical meaning of the linear sampling method,” in *Proc. 6th Eur. Conf. Antennas Propag. (EUCAP)*, Mar. 2012, pp. 3210–3214.
- [11] L. Crocco and T. Isernia, “Inverse scattering with real data: Detecting and imaging homogeneous dielectric objects,” *Inverse Prob.*, vol. 17, no. 6, p. 1573, 2001.
- [12] A. M. Hassan, T. C. Bowman, and M. El-Shenawee, “Efficient microwave imaging algorithm based on hybridization of the linear sampling and level set methods,” *IEEE Trans. Antennas Propag.*, vol. 61, no. 7, pp. 3765–3773, Jul. 2013.
- [13] I. Catapano, A. Randazzo, E. Slob, and R. Solimene, “GPR imaging via qualitative and quantitative approaches,” in *Civil Engineering Applications of Ground Penetrating Radar*, A. Benedetto and L. Pajewski, Eds. Cham, Switzerland: Springer, 2015, pp. 239–280.
- [14] L. L. Monte, F. Soldovieri, D. Erricolo, and M. C. Wicks, “Imaging below irregular terrain using RF tomography,” *IEEE Trans. Geosci. Remote Sens.*, vol. 50, no. 9, pp. 3364–3373, Sep. 2012.
- [15] M. Pastorino *et al.*, “A microwave tomographic system for wood characterization in the forest products industry,” *Wood Mater. Sci. Eng.*, vol. 10, no. 1, pp. 75–85, 2015.
- [16] F. Soldovieri, R. Solimene, and G. Prisco, “A multiarray tomographic approach for through-wall imaging,” *IEEE Trans. Geosci. Remote Sens.*, vol. 46, no. 4, pp. 1192–1199, Apr. 2008.
- [17] L. L. Monte, D. Erricolo, F. Soldovieri, and M. C. Wicks, “Radio frequency tomography for tunnel detection,” *IEEE Trans. Geosci. Remote Sens.*, vol. 48, no. 3, pp. 1128–1137, Mar. 2010.
- [18] A. Afsari, A. M. Abbosh, and Y. Rahmat-Samii, “A rapid medical microwave tomography based on partial differential equations,” *IEEE Trans. Antennas Propag.*, vol. 66, no. 10, pp. 5521–5535, Oct. 2018.
- [19] K. Ren, Q. Wang, and R. J. Burkholder, “A fast back-projection approach to diffraction tomography for near-field microwave imaging,” *IEEE Antennas Wireless Propag. Lett.*, vol. 18, no. 10, pp. 2170–2174, Oct. 2019.
- [20] W. Zhang and A. Hoofar, “Three-dimensional real-time through-the-wall radar imaging with diffraction tomographic algorithm,” *IEEE Trans. Geosci. Remote Sens.*, vol. 51, no. 7, pp. 4155–4163, Jul. 2013.
- [21] L. Zhang, H.-L. Li, Z.-J. Qiao, and Z.-W. Xu, “A fast BP algorithm with wavenumber spectrum fusion for high-resolution spotlight SAR imaging,” *IEEE Geosci. Remote Sens. Lett.*, vol. 11, no. 9, pp. 1460–1464, Sep. 2014.
- [22] G. Jia, M. Buchroithner, W. Chang, and X. Li, “Simplified real-time imaging flow for high-resolution FMCW SAR,” *IEEE Geosci. Remote Sens. Lett.*, vol. 12, no. 5, pp. 973–977, May 2015.
- [23] D. Henke, E. M. Dominguez, D. Small, M. E. Schaepman, and E. Meier, “Moving target tracking in single- and multichannel SAR,” *IEEE Trans. Geosci. Remote Sens.*, vol. 53, no. 6, pp. 3146–3159, Jun. 2015.
- [24] Y. M. Wang and W. C. Chew, “An iterative solution of the two-dimensional electromagnetic inverse scattering problem,” *Int. J. Imag. Syst. Technol.*, vol. 1, no. 1, pp. 100–108, 1989.
- [25] Y. Zhong and X. Chen, “An FFT twofold subspace-based optimization method for solving electromagnetic inverse scattering problems,” *IEEE Trans. Antennas Propag.*, vol. 59, no. 3, pp. 914–927, Mar. 2011.
- [26] K. Xu, Y. Zhong, and G. Wang, “A hybrid regularization technique for solving highly nonlinear inverse scattering problems,” *IEEE Trans. Microw. Theory Techn.*, vol. 66, no. 1, pp. 11–21, Jan. 2018.
- [27] T. M. Habashy, M. L. Oristaglio, and A. T. de Hoop, “Simultaneous nonlinear reconstruction of two-dimensional permittivity and conductivity,” *Radio Sci.*, vol. 29, no. 4, pp. 1101–1118, 1994.
- [28] P. M. van den Berg and R. E. Kleinman, “A contrast source inversion method,” *Inverse Problems*, vol. 13, no. 6, pp. 1607–1620, Dec. 1997.
- [29] P. M. van den Berg, A. L. V. Broekhoven, and A. Abubakar, “Extended contrast source inversion,” *Inverse Problems*, vol. 15, no. 5, pp. 1325–1344, 1999.

- [30] X. Chen, "Subspace-based optimization method for solving inverse-scattering problems," *IEEE Trans. Geosci. Remote Sens.*, vol. 48, no. 1, pp. 42–49, Jan. 2010.
- [31] M. Pastorino, A. Massa, and S. Caorsi, "A microwave inverse scattering technique for image reconstruction based on a genetic algorithm," *IEEE Trans. Instrum. Meas.*, vol. 49, no. 3, pp. 573–578, Jun. 2000.
- [32] A. Qing, C. K. Lee, and L. Jen, "Electromagnetic inverse scattering of two-dimensional perfectly conducting objects by real-coded genetic algorithm," *IEEE Trans. Geosci. Remote Sens.*, vol. 39, no. 3, pp. 665–676, Mar. 2001.
- [33] R. A. Wildman and D. S. Weile, "Geometry reconstruction of conducting cylinders using genetic programming," *IEEE Trans. Antennas Propag.*, vol. 55, no. 3, pp. 629–636, Mar. 2007.
- [34] M. Donelli, D. Franceschini, P. Rocca, and A. Massa, "Three-dimensional microwave imaging problems solved through an efficient multiscaling particle swarm optimization," *IEEE Trans. Geosci. Remote Sens.*, vol. 47, no. 5, pp. 1467–1481, May 2009.
- [35] M. Salucci, L. Poli, N. Anselmi, and A. Massa, "Multifrequency particle swarm optimization for enhanced multiresolution GPR microwave imaging," *IEEE Trans. Geosci. Remote Sens.*, vol. 55, no. 3, pp. 1305–1317, Mar. 2017.
- [36] S. Caorsi, M. Donelli, A. Lommi, and A. Massa, "Location and imaging of two-dimensional scatterers by using a particle swarm algorithm," *J. Electromagn. Waves Appl.*, vol. 18, no. 4, pp. 481–494, Jan. 2004.
- [37] S. Caorsi, A. Massa, M. Pastorino, M. Raffetto, and A. Randazzo, "Detection of buried inhomogeneous elliptic cylinders by a memetic algorithm," *IEEE Trans. Antennas Propag.*, vol. 51, no. 10, pp. 2878–2884, Oct. 2003.
- [38] M. Pastorino, "Stochastic optimization methods applied to microwave imaging: A review," *IEEE Trans. Antennas Propag.*, vol. 55, no. 3, pp. 538–548, Mar. 2007.
- [39] S. Caorsi and P. Gamba, "Electromagnetic detection of dielectric cylinders by a neural network approach," *IEEE Trans. Geosci. Remote Sens.*, vol. 37, no. 2, pp. 820–827, Mar. 1999.
- [40] I. T. Rekanos, "Neural-network-based inverse-scattering technique for online microwave medical imaging," *IEEE Trans. Magn.*, vol. 38, no. 2, pp. 1061–1064, Mar. 2002.
- [41] L. Li, L. G. Wang, F. L. Teixeira, C. Liu, A. Nehorai, and T. J. Cui, "DeepNIS: Deep neural network for nonlinear electromagnetic inverse scattering," *IEEE Trans. Antennas Propag.*, vol. 67, no. 3, pp. 1819–1828, Mar. 2019.
- [42] Z. Wei and X. Chen, "Deep-learning schemes for full-wave nonlinear inverse scattering problems," *IEEE Trans. Geosci. Remote Sens.*, vol. 57, no. 4, pp. 1849–1860, Apr. 2019.
- [43] J. Xiao, J. Li, Y. Chen, F. Han, and Q. H. Liu, "Fast electromagnetic inversion of inhomogeneous scatterers embedded in layered media by born approximation and 3-D U-Net," *IEEE Geosci. Remote Sens. Lett.*, vol. 17, no. 10, pp. 1677–1681, Oct. 2020, doi: 10.1109/LGRS.2019.2953708.
- [44] G.-B. Huang, Q.-Y. Zhu, and C.-K. Siew, "Extreme learning machine: Theory and applications," *Neurocomputing*, vol. 70, nos. 1–3, pp. 489–501, Dec. 2006.
- [45] L.-Y. Xiao, J. Li, F. Han, W. Shao, and Q. H. Liu, "Dual-module NMM-IEM machine learning for fast electromagnetic inversion of inhomogeneous scatterers with high contrasts and large electrical dimensions," *IEEE Trans. Antennas Propag.*, vol. 68, no. 8, pp. 6245–6255, Aug. 2020.
- [46] F. Li, Q. H. Liu, and L.-P. Song, "Three-dimensional reconstruction of objects buried in layered media using Born and distorted Born iterative methods," *IEEE Geosci. Remote Sens. Lett.*, vol. 1, no. 2, pp. 107–111, Apr. 2004.
- [47] W. Zhang and Q. H. Liu, "Three-dimensional scattering and inverse scattering from objects with simultaneous permittivity and permeability contrasts," *IEEE Trans. Geosci. Remote Sens.*, vol. 53, no. 1, pp. 429–439, Jan. 2015.
- [48] K. A. Michalski and J. R. Mosig, "Multilayered media Green's functions in integral equation formulations," *IEEE Trans. Antennas Propag.*, vol. 45, no. 3, pp. 508–519, Mar. 1997.
- [49] X. M. Xu and Q. H. Liu, "The BCGS-FFT method for electromagnetic scattering from inhomogeneous objects in a planarly layered medium," *IEEE Antennas Wireless Propag. Lett.*, vol. 1, no. 1, pp. 77–80, 2002.
- [50] G.-B. Huang, Q.-Y. Zhu, and C.-K. Siew, "Extreme learning machine: A new learning scheme of feedforward neural networks," in *Proc. IEEE Int. Joint Conf. Neural Netw.*, Budapest, Hungary, Jul. 2004, pp. 25–29.
- [51] S. Tamura and M. Tateishi, "Capabilities of a four-layered feedforward neural network: Four layers versus three," *IEEE Trans. Neural Netw.*, vol. 8, no. 2, pp. 251–255, Mar. 1997.
- [52] G.-B. Huang, "Learning capability and storage capacity of two-hidden-layer feedforward networks," *IEEE Trans. Neural Netw.*, vol. 14, no. 2, pp. 274–281, Mar. 2003.
- [53] R. Hecht-Nielsen, "Kolmogorov's mapping neural network existence theorem," in *Proc. IEEE Conf. Neural Netw.*, New York, NY, USA, Jun. 1987, pp. 11–13.
- [54] P. Arena, L. Fortuna, R. Re, and M. G. Xibilia, "Multilayer perceptrons to approximate complex valued functions," *Int. J. Neural Syst.*, vol. 6, no. 4, pp. 435–446, Dec. 1995.
- [55] M.-B. Li, G.-B. Huang, P. Saratchandran, and N. Sundararajan, "Fully complex extreme learning machine," *Neurocomputing*, vol. 68, nos. 1–4, pp. 306–314, Oct. 2005.
- [56] G.-B. Huang, M.-B. Li, L. Chen, and C.-K. Siew, "Incremental extreme learning machine with fully complex hidden nodes," *Neurocomputing*, vol. 71, nos. 4–6, pp. 576–583, 2008.
- [57] T. J. Cui, W. C. Chew, X. X. Yin, and W. Hong, "Study of resolution and super resolution in electromagnetic imaging for half-space problems," *IEEE Trans. Antennas Propag.*, vol. 52, no. 6, pp. 1398–1411, Jun. 2004.
- [58] J. M. Geffrin and P. Sabouroux, "Continuing with the Fresnel database: Experimental setup and improvements in 3D scattering measurements," *Inverse Probl.*, vol. 25, no. 2, pp. 1–18, Feb. 2009.
- [59] C. Yu, M. Yuan, and Q. H. Liu, "Reconstruction of 3D objects from multi-frequency experimental data with a fast DBIM-BCGS method," *Inverse Probl.*, vol. 25, no. 2, pp. 1–24, Feb. 2009.



**Li-Ye Xiao** (Member, IEEE) received the B.S. and Ph.D. degrees in electronic information science and technology from the University of Electronic Science and Technology of China (UESTC), Chengdu, China, in 2015 and 2019, respectively.

In 2018, he was a Visiting Scholar with the Department of Electrical and Computer Engineering, Duke University, Durham, NC, USA. He joined the Institute of Electromagnetics and Acoustics, Xiamen University, Xiamen, China, in 2019, where he is currently an Associate Professor. His research interest is computational electromagnetics.

**Jiawen Li**, photograph and biography not available at the time of publication.

**Feng Han**, photograph and biography not available at the time of publication.

**Hao-Jie Hu**, photograph and biography not available at the time of publication.

**Mingwei Zhuang**, photograph and biography not available at the time of publication.

**Qing Huo Liu**, photograph and biography not available at the time of publication.